Compartment model-based nonlinear unmixing for kinetic analysis of dynamic PET images

Yanna Cruz Cavalcanti, Thomas Oberlin, Vinicius Ferraris, Nicolas Dobigeon, Maria Ribeiro, Clovis Tauber

▶ **To cite this version:**

Yanna Cruz Cavalcanti, Thomas Oberlin, Vinicius Ferraris, Nicolas Dobigeon, Maria Ribeiro, et al.. Compartment model-based nonlinear unmixing for kinetic analysis of dynamic PET images. Medical Image Analysis, 2023, 84, pp.102689. 10.1016/j.media.2022.102689 . hal-03928633

HAL Id: hal-03928633
https://hal.science/hal-03928633

Submitted on 7 Jan 2023

HAL is a multi-disciplinary open access archive for the deposit and dissemination of scientific research documents, whether they are published or not. The documents may come from teaching and research institutions in France or abroad, or from public or private research centers.

L'archive ouverte pluridisciplinaire **HAL**, est destinée au dépôt et à la diffusion de documents scientifiques de niveau recherche, publiés ou non, émanant des établissements d'enseignement et de recherche français ou étrangers, des laboratoires publics ou privés.

Compartment Model-based Nonlinear Unmixing for Kinetic Analysis of Dynamic PET Images

Yanna Cruz Cavalcanti[a,*], Thomas Oberlin[b], Vinicius Ferraris[a], Nicolas Dobigeon[a,c], Maria Ribeiro[d], Clovis Tauber[d]

[a] *University of Toulouse, IRIT/INP-ENSEEIHT, 31071 Toulouse Cedex 7, France*
[b] *ISAE-SUPAERO, University of Toulouse, France*
[c] *Institut Universitaire de France (IUF), France*
[d] *UMRS Inserm U930 - Université de Tours, 37032 Tours, France*

Abstract

When no arterial input function is available, quantification of dynamic PET images requires a previous step devoted to the extraction of a reference time-activity curve (TAC). Factor analysis is often applied for this purpose. This paper introduces a novel approach that conducts a new kind of nonlinear factor analysis relying on a compartment model, and computes the kinetic parameters of specific binding tissues jointly. To this end, it capitalizes on data-driven parametric imaging methods to provide a physical description of the underlying PET data, directly relating the specific binding with the kinetics of the non-specific binding in the corresponding tissues. This characterization is introduced into the factor analysis formulation to yield a novel nonlinear unmixing model designed for PET image analysis. This model also explicitly introduces global kinetic parameters that allow for a direct estimation of a binding potential that represents the ratio at equilibrium of specifically bound radioligand to the concentration of nondisplaceable radioligand in each non-specific binding tissue. The performance of the method is evaluated on

[☆] Part of this work has been funded by the ANR-3IA Artificial and Natural Intelligence Toulouse Institute (ANITI).

[*] Corresponding author

Email addresses: yanna.cavalcanti@enseeiht.fr (Yanna Cruz Cavalcanti), thomas.oberlin@isae-supaero.fr (Thomas Oberlin), vinicius.ferraris@enseeiht.fr (Vinicius Ferraris), nicolas.dobigeon@enseeiht.fr (Nicolas Dobigeon), maria.ribeiro@univ-tours.fr (Maria Ribeiro), clovis.tauber@univ-tours.fr (Clovis Tauber)

synthetic and real data to demonstrate its potential interest.

1. Introduction

Dynamic positron emission tomography (PET) is an imaging technique delivering relevant information on physiological dysfunctions preceding appearance of morphological abnormalities such as cancer and dementia. To provide interpretable results, PET images have to pass through a process called quantification (Buvat, 2007). It consists in exploring the variations of the concentration of radiotracers over time, characterized by time-activity curves (TACs), in order to estimate the kinetic parameters that describe the studied process. Most of the quantification techniques that are used in practice require an estimation of reference TACs representing tissues (Blomqvist et al., 1989; Cunningham et al., 1991). In this context, many methods were developed to perform a non-invasive extraction of the global kinetics of a tracer, in particular factor analysis (Barber, 1980; Cavailloles et al., 1984). More recently, deep learning (DL) techniques have been considered to tackle this problem, either with the estimation of macro-parameters with no need for an input function as in Wang et al. (2020), or with the direct quantification of the image as in Polymeri et al. (2020). For the latter case, DL-based methods generally require large training data sets covering a large variety of sample subjects for each possible scan setting and radiotracer. Conversely, unsupervised methods such as the factor analysis proposed in this work fully exploit physically-based models and additional prior knowledge, and their applicability are not constrained by the availability of large labeled data sets.

However, standard factor analysis techniques rely on the assumption that the elementary response of each tissue to tracer distribution is spatially homogeneous. To overcome this limitation, Cavalcanti et al. (2018) introduced a factor analysis model that handled fluctuations in specific binding (SB) kinetics with a spatially indexed variability. The proposed model tried to extract a factor for the blood input function, a factor for each non-specific binding (nSB) tissue

of the region under study and assigned a spatially varying factor for high-uptake tissues.

Furthermore, the kinetics of the ligand in SB tissues are often related to those in nSB tissues, as considered by the reference tissue input models from the quantification literature (Lammertsma and Hume, 1996). Indeed, when targets are present, the kinetics of the radioligand in a tissue that is non-specific under healthy circumstances will be nonlinearly modified, though it is still the same tissue or organ. Therefore, this work proposes to study SB kinetics as an instance of the nSB ones. The main idea is to perform factor analysis on nSB tissues and blood while allowing for nonlinearities on each nSB tissue that will describe the SB part present in these regions.

Ideally, these nonlinearities should directly provide an interpretable result in terms of quantification, representing different levels of binding. To do so, one resorts to the parametric pharmacokinetic models discussed by Gunn et al. (2001). They are shown to be very useful for providing physiologically meaningful analysis of PET data. Conventional methods used for kinetic parameter estimation often define a region-of-interest (ROI) and then perform estimation based on the ROI average (Lammertsma and Hume, 1996; Berti et al., 2010). These approaches neglect any spatial variations in the tracer kinetics within the ROI, e.g., due to inhomogeneous distribution of the target, existence of sub-regions, partial volume effects (PVE) or tissue heterogeneity. To avoid this homogeneous ROI assumption, some studies performed a voxel-by-voxel estimation of kinetic parameters and, to overcome poor signal-to-noise ratio (SNR), applied additional penalizations to stabilize the estimation (Kamasak et al., 2005; Huang and Zhou, 1998). For instance, Gunn et al. (2002) defined basis functions to model the kinetics of the tracer. The basis functions are pre-computed and an undetermined system of equations is solved to fit to the data with a technique named DEPICT. Since this is an ill-posed problem, an additional sparsity penalization is imposed to the basis coefficients. This sparsity assumption is motivated by the fact that data is expected to be described by a few compartments. Peng et al. (2008) investigated the use

of sparse Bayesian learning for parametric estimation, further allowing the coefficients to be nonnegative, in agreement with reference tissue models.

Nevertheless, these approaches still assume that there is only one kinetic process occurring per voxel whereas, due to the low spatial resolution, the PVE and the biological heterogeneity, the resulting signal is often a mixture of multiple kinetic processes. This is also the rationale behind several factor analysis models proposed in the literature (Paola et al., 1982; Sitek et al., 2000). To overcome this limitation, Lin et al. (2014) proposed a two-stage algorithm that benefits from prior information provided by parametric imaging models on the physics and physiology of metabolism while introducing partial volume with a linear combination of the different kinetics. The first step consisted in a dictionary-based estimation of the nonlinear kinetics of each considered tissue and the second step computed the tissue fractions and the linear terms of the tissue kinetic models. This model considers that each image voxel is described by a linear mixing of K classes, including blood, and assumes that the blood input function $\mathbf{m}_K$ is known. Each tissue factor TAC $\mathbf{m}_k(\boldsymbol{\kappa})$, for $k = 1, \cdots, K-1$, is described by a three-tissue compartment model (Huang et al., 1980) with kinetic parameters $\boldsymbol{\kappa}$. The final formulation for each voxel can be written as

$$\mathbf{x}_n = \sum_{k=1}^{K-1} a_{kn}\mathbf{m}_k(\boldsymbol{\kappa}) + a_{Kn}\mathbf{m}_K. \tag{1}$$

A similar approach was also proposed by Chen et al. (2011). Based on the same idea, Klein et al. (2010) tried to describe each factor TAC with an input function-based kinetic model and to jointly estimate this input function as well as the model parameters for each factor.

However, many experimental results indicate that the use of commonly accepted multi-compartment models often leads to considerably biased and high-variance estimates of the pharmacokinetics parameters, due to the high number of parameters to be estimated (Padhani and Husband, 2001; Padhani, 2003; Buckley, 2002). Moreover, they often oversimplify the kinetics of several tracers, especially in case of tissue heterogeneity (DeLorenzo et al., 2009). As an attempt at providing a more accurate description of the kinetics of the tracer

while benefiting from the physiological description of parametric imaging, the approach proposed in this paper relies on a parametric nonlinear factor analysis. Differently from the approach followed by Lin et al. (2014), factor TACs from nSB tissues will be directly estimated in the model and, based on the data-driven reference input model by Gunn et al. (2002), will be used as reference tissue TACs for the recovery of the kinetic parameters from SB. The idea of linking factor analysis to compartmental modeling has already been investigated by some works from the PET literature. In particular, Nijran and Barber (1985) proposed to constrain the space of possible solutions of factor analysis with the space of theoretical solutions given by compartmental models. Szabo et al. (1993) used factor analysis to differentiate SB and nSB TACs and determine the number of compartments needed to model the kinetics of [11C] pyrilamine in the brain. El Fakhri et al. (2005, 2009) used a previous factor analysis step to extract the input functions that were used to compute the TACs in each voxel with a two-compartment model. The work proposed in this article goes one step further by jointly conducting factor and kinetic analysis. This paper is organized as follows. Section 2 provides the theory that underlies this work. The proposed nonlinear model and the corresponding unmixing framework are introduced in Section 3. Results from simulations conducted on synthetic and real image are reported in Section 4 and Section 5, respectively. The proposed method, its rationale, some pitfalls and some assets are discussed in Section 6. Section 7 concludes the paper.

2. Background

2.1. Nonlinear mixing models

Let $\mathbf{x}_n \in \mathbb{R}^L$ be the nth voxel TAC neglecting any measurement noise, where L is the number of time-frames. Linear mixing models (LMM), which are the basis of factor analysis, assume each TAC to be a linear combination of K elementary factors $\mathbf{m}_k \in \mathbb{R}^L$ and their respective mixing coefficients a_{kn} (Bioucas-Dias et al., 2012; Dobigeon et al., 2009). More explicitly, this model

is mathematically expressed as

$$\mathbf{x}_n = \sum_{k=1}^{K} a_{kn}\mathbf{m}_k = \mathbf{M}\mathbf{a}_n \tag{2}$$

with $\mathbf{M} = [\mathbf{m}_1, \ldots, \mathbf{m}_K]$ and $\mathbf{a}_n = [a_{1n}, \ldots, a_{Kn}]$. Moreover, non-negativity constraints are assumed for the factors $\mathbf{m}_k = [m_{1,k}, \ldots, m_{L,k}]^T$, i.e.,

$$m_{lk} \geq 0 \tag{3}$$

while factor proportions are constrained to be non-negative and sum to one

$$a_{k,n} \geq 0 \quad \text{and} \quad \sum_{k=1}^{K} a_{kn} = 1. \tag{4}$$

When nonlinearities are present, this model is no longer sufficient to describe the behavior of the TACs. To overcome this issue, several nonlinear mixing models and their corresponding unmixing algorithms were proposed, raising a fertile branch of research in hyperspectral imaging for Earth observation (Heylen et al., 2014; Dobigeon et al., 2014b,a). A large family of nonlinear models can be described as (Altmann et al., 2011; Meganem et al., 2014; Eches and Guillaume, 2014)

$$\mathbf{x}_n = \mathbf{M}\mathbf{a}_n + \boldsymbol{\mu}(\mathbf{M}, \mathbf{a}_n, \mathbf{b}_n), \tag{5}$$

where, in addition to the linear contribution in (2), the observed pixel is also composed of an additive nonlinear term $\boldsymbol{\mu}(\cdot)$ that may depend on the factors matrix $\mathbf{M}$, the factor proportion coefficients $\mathbf{a}_n$ and new additional nonlinearities coefficients $\mathbf{b}_n$. The rationale behind the relation between the nonlinear coefficients and the amount of linear contributions a_{kn} comes from the fact that a pixel containing more of a given factor is more subjected to nonlinear interactions. In other words, if a material is not present in one pixel, it cannot interact with other materials (Fan et al., 2009).

2.2. Reference tissue input models

Tracer kinetic modelling techniques are used to estimate biologically interpretable parameters by describing the TACs in a ROI with mathematical models. A wide range of techniques model the PET signals based on compartmental analysis of the tracer (Gunn et al., 2001). These approaches

may be divided into two major groups: model-driven methods and data-driven methods (Gunn et al., 2002). Model-driven methods are based on a previously chosen compartmental model, whereas data-driven techniques do not need any *a priori* decisions about the most appropriate model structure.

In this work, we will be specially interested in the general model based on reference tissues developed by Gunn et al. (2002). It relies on a basis function framework and it does not require any knowledge on the compartment model. Each target voxel TAC is described as

$$\mathbf{x}_n(\mathbf{b}_n, \boldsymbol{\alpha}) = \left((1 + b_{0n})\delta(\mathbf{t}) + \sum_{i=1}^{V} b_{in} e^{-\alpha_i \mathbf{t}} \right) * \mathbf{m}_{\mathrm{R}}, \tag{6}$$

where V is the total number of tissue compartments in both the target and reference tissues, $\mathbf{t} = [t_1, \cdots, t_L]^T$ are the times of acquisition which are assumed to be known, $*$ stands for temporal convolution, $\delta(\mathbf{t})$ is the Dirac impulse function and $e^{\boldsymbol{\theta}}$ is a point-wise exponentiation. As before, $\mathbf{x}_n$ denotes the TAC in the nth voxel, while $\mathbf{m}_{\mathrm{R}}$ is the reference tissue TAC of the studied ROI, and the new variables $\mathbf{b}_n = [b_{1n}, \ldots, b_{Vn}]$ and $\boldsymbol{\alpha} = [\alpha_1, \ldots, \alpha_V]$ describe the kinetics of the tracer. This formulation neglects the blood volume in both target and reference tissues. For models with reversible target tissue kinetics ($\alpha_i > 0$), Gunn et al. (2001) derived a direct relation for the ratio at equilibrium of specifically bound radioligand to that of nondisplaceable radioligand in tissue (see Innis et al. (2007)), denoted $\mathrm{BP_{ND}}$ and given by

$$\mathrm{BP_{ND}} = b_{0n} + \sum_{i=1}^{V} \frac{b_{in}}{\alpha_i}. \tag{7}$$

The tracer delivery ratio between the nth targeted voxel and the reference region is given by $R_{1n} = 1 + b_{0n}$. The use of 1 in eq (6) is to simplify further equations of the model. The only difference with the usual notation is that (7) express directly the $\mathrm{BP_{ND}}$ rather than the distribution volume ratio. More details are given in Appendix A.

3. Proposed framework

3.1. Nonlinear PNMM model

The proposed framework combines the model in (6) with the generalization of the linear mixing (1) by associating each reference TAC to a nSB tissue TAC, except for the blood factor TAC $\mathbf{m}_K$. This yields the following so-called parametric nonlinear mixing model (PNMM)

$$\mathbf{x}_n = \sum_{k=1}^{K-1} a_{kn} \left(\mathbf{m}_k + \sum_{i=1}^{V} b_{kin} \mathbf{m}_k * e^{-\alpha_{ki}\mathbf{t}} + b_{k0n} \mathbf{m}_k \right) + a_{Kn} \mathbf{m}_K \tag{8}$$

where b_{kin} receives an additional index k since this coefficient is now specific to each reference tissue TAC. This model is expected to be more flexible than the previous ones, since it accounts for possible PVE induced by mixing between tissues and blood, while benefiting from the physical considerations of parametric imaging. It also directly estimates the global kinetics of one tissue, thus not being completely dependent of kinetic parameters. This can offer a more precise quantification as it automatically analyses different nSB tissues separately, accounting implicitly for possible differences in perfusion of such tissues. It may also allow the tissue affected by SB to be identified, through the computation of the BP within each nSB tissue.

Adopting matrix notations consistent with those introduced in Section 2.1, the noise-free image $\mathbf{X} \in \mathbb{R}^{L \times N}$ writes

$$\mathbf{X} = \mathbf{M}\mathbf{A} + \sum_{i=0}^{V} \mathbf{Q}_i (\tilde{\mathbf{A}} \circ \mathbf{B}_i) \tag{9}$$

where $\mathbf{M}$ is a $L \times K$ matrix containing the factor TACs, $\mathbf{A}$ is a $K \times N$ matrix composed of the factor proportion vectors $\mathbf{a}_n = [a_{1n}, \ldots, a_{Kn}]^T$ and $\circ$ is the Hadamard point-wise product. The matrix $\tilde{\mathbf{A}}$ denotes the factor proportion matrix while omitting the blood, i.e., composed of vectors $\tilde{\mathbf{a}}_n = [a_{1n}, \ldots, a_{K-1,n}]^T$. The kinetic parameters are encoded in the matrices $\mathbf{Q}_i$, with $i \in \{0, \ldots, V\}$, depending on $\mathbf{M}$ and $\boldsymbol{\alpha}$,

$$\mathbf{Q}_i = \left[\mathbf{m}_1 * e^{-\alpha_{1i}\mathbf{t}} \quad \cdots \quad \mathbf{m}_{K-1} * e^{-\alpha_{(K-1)i}\mathbf{t}} \right]. \tag{10}$$

Furthermore, the convolution operator in (10) can be replaced by a product by Toeplitz matrix defined by the vectors $e^{-\alpha_{ki}\mathbf{t}}$ (Chen et al., 2011), i.e.,

$$\mathbf{Q}_i = \begin{bmatrix} \mathbf{E}_{1i}\mathbf{m}_1 & \cdots & \mathbf{E}_{(K-1)i}\mathbf{m}_{K-1} \end{bmatrix}. \tag{11}$$

with

$$\mathbf{E}_{ki} = T_p(e^{-\alpha_{ki}\mathbf{t}}), \tag{12}$$

where T_p is the operator that transforms a vector into a symmetric Toeplitz matrix whose dimensions are defined by the vector length. Note that, $\forall k \in \{1, \ldots, K-1\}$, $\alpha_{k0} = 0$ and thus $\mathbf{E}_{k0} = \mathbf{I}_L$ and $\mathbf{Q}_0 = [\mathbf{m}_1, \cdots, \mathbf{m}_{K-1}]$. Also, the matrices of internal coefficients related to the basis functions are given by

$$\mathbf{B}_i = \begin{bmatrix} b_{1i1} & b_{1i2} & \cdots & b_{1iN} \\ b_{2i1} & b_{2i2} & \cdots & b_{2iN} \\ \vdots & \vdots & \vdots & \vdots \\ b_{(K-1)i1} & b_{(K-1)i2} & \cdots & b_{(K-1)iN} \end{bmatrix}, \tag{13}$$

with $\underline{\mathbf{B}} = \{\mathbf{B}_0, \ldots, \mathbf{B}_V\}$.

Besides, additional constraints regarding these sets of parameters are assumed. As in (3) and (4), non-negativity is assumed for the factors and corresponding proportions sum to one to reflect physical considerations. Moreover, according to Gunn et al. (2002), to reduce the indeterminacy of the basis elements solution while allowing for a suitable coverage of the kinetic spectrum, the elements of $\boldsymbol{\alpha}_i = \begin{bmatrix} \alpha_{1i} & \cdots & \alpha_{(K-1)i} \end{bmatrix}$ are assumed to be lower- and upper-bounded by predefined values adjusting the range of expected values. Thus, the kinetic parameter vector $\boldsymbol{\alpha}_i$ ($\forall i \in \{1, \ldots, V\}$) are assumed to belong to the set

$$\boldsymbol{\alpha}_i \in \mathcal{R} \triangleq \{\mathbf{z} \in \mathbb{R}^{K-1} : \alpha_i^{\min} \preceq z_k \preceq \alpha_i^{\max}\}. \tag{14}$$

A similar choice is adopted for the internal weights, i.e.,

$$\mathbf{B}_i \in \mathcal{B} \triangleq \{\mathbf{z} \in \mathbb{R}^{(K-1)\times N} : b_i^{\min} \preceq z_{kn} \preceq b_i^{\max}\}. \tag{15}$$

The range of the admissible values for the kinetic parameters defined by the constraints (14) and (15) should be adjusted w.r.t. prior knowledge regarding

the experimental setting, such as the acquisition protocol (e.g., the properties of the radiotracer), the possible pathology under study and the very nature of the analyzed PET images, in particular when they have been post-processed before conducting the proposed nonlinear unmixing. This point has been further discussed in Section 6.

3.2. Corresponding optimization problem

The PNMM (9) and constraints (3), (4), (14) and (15) are combined to formulate a constrained optimization problem. A cost function is thereby defined to estimate the matrices $\mathbf{M}$, $\mathbf{A}$ and $\boldsymbol{\alpha}$ and the set $\underline{\mathbf{B}}$ containing the matrices $\mathbf{B}_i$. For the data-fidelity term, we choose the squared Frobenius distance between the dynamic PET image $\mathbf{Y}$ and the proposed data modeling $\mathbf{X}$ defined by PNMM in (9), implicitly assuming Gaussian noise. Since the problem is ill-posed and nonconvex, additional regularizers become essential. In this work, we propose to define penalization functions $\boldsymbol{\Psi}$, $\boldsymbol{\Phi}$ and $\boldsymbol{\Omega}$ to reflect the available *prior* knowledge on $\mathbf{M}$, $\mathbf{A}$ and $\underline{\mathbf{B}}$, respectively. The optimization problem is then defined as

$$(\mathbf{M}^*, \mathbf{A}^*, \underline{\mathbf{B}}^*, \boldsymbol{\alpha}^*) \in \underset{\mathbf{M},\mathbf{A},\underline{\mathbf{B}},\boldsymbol{\alpha}}{\arg\min}\, \mathcal{J}(\mathbf{M}, \mathbf{A}, \underline{\mathbf{B}}, \boldsymbol{\alpha}) \tag{16}$$

with

$$\begin{aligned}\mathcal{J}(\mathbf{M}, \mathbf{A}, \underline{\mathbf{B}}, \boldsymbol{\alpha}) = \frac{1}{2} \left\| \mathbf{Y} - \mathbf{M}\mathbf{A} - \sum_{i=0} \mathbf{Q}_i(\tilde{\mathbf{A}} \circ \mathbf{B}_i) \right\|_{\mathrm{F}}^2 \\ + \beta\boldsymbol{\Psi}(\mathbf{M}) + \eta\boldsymbol{\Phi}(\mathbf{A}) + \lambda\boldsymbol{\Omega}(\underline{\mathbf{B}}) \\ + \imath_{\mathbb{R}_+^{L\times K}}(\mathbf{M}) + \imath_{\mathcal{A}}(\mathbf{A}) + \imath_{\mathcal{R}^{V+1}}(\boldsymbol{\alpha}) + \imath_{\mathcal{B}^{V+1}}(\underline{\mathbf{B}})\end{aligned} \tag{17}$$

where the parameters η, β and λ adjust the regularizations $\boldsymbol{\Phi}(\mathbf{A})$, $\boldsymbol{\Psi}(\mathbf{M})$ and $\boldsymbol{\Omega}(\underline{\mathbf{B}})$ and $\imath_{\cdot}(\cdot)$ denotes the indicator function on the feasible set associated with the parameter constraints. As already proposed by Cavalcanti et al. (2018), the penalizations $\boldsymbol{\Psi}(\mathbf{M})$ and $\boldsymbol{\Phi}(\mathbf{A})$ associated with factor TACs and factor proportions are chosen to promote short distances to rough factor TAC estimates and spatially smooth abundance maps, respectively. The penalization function

for the variable $\underline{\mathbf{B}}$ is assumed to be separable with respect to (w.r.t.) the tissue compartment, i.e.,

$$\boldsymbol{\Omega}(\underline{\mathbf{B}}) = \sum_{i=0}^{V} \Omega_i(\mathbf{B}_i), \tag{18}$$

where $\Omega_i(\mathbf{B}_i)$ promotes spatial sparsity through a group lasso regularizer defined as (Cavalcanti et al., 2019; Ferraris et al., 2017)

$$\Omega_i(\mathbf{B}_i) = \|\mathbf{B}_i\|_{2,1} = \sum_{n=1}^{N} \|\mathbf{b}_{in}\|_2. \tag{19}$$

The choice of these penalization functions, in particular w.r.t. to $\underline{\mathbf{B}}$, are driven by the applicative scenario that will be considered in the experiments reported in Sections 4 and 5. This choice is further discussed in Section 6.

3.3. Optimization with PALM

As the optimization problem (16) is nonconvex and nonsmooth, the chosen minimization strategy is the proximal alternating linearized minimization (PALM) scheme (Bolte et al., 2013). It consists in iteratively updating each variable $\mathbf{A}$, $\mathbf{M}$, $\underline{\mathbf{B}}$ and $\boldsymbol{\alpha}$ while all the others are fixed, finally converging to a local critical point $\mathbf{A}^*$, $\mathbf{M}^*$, $\underline{\mathbf{B}}^*$ and $\boldsymbol{\alpha}^*$. The resulting unmixing algorithm, whose main steps are described in the following paragraphs, is summarized in Algo. 1. More details regarding each step are reported in Appendix B to Appendix E.

3.3.1. Optimization with respect to $\mathbf{M}$

A direct application of the scheme introduced by Bolte et al. (2013) under the constraints defined by (3) leads to the following updating rule

$$\mathbf{M} = \mathcal{P}_+\left(\mathbf{M} - \frac{\gamma}{L_M}\nabla_{\mathbf{M}}\mathcal{J}(\mathbf{M}, \mathbf{A}, \underline{\mathbf{B}}, \boldsymbol{\alpha})\right) \tag{20}$$

where $\mathcal{P}_+(\cdot)$ is the projector onto the nonnegative set $\{\mathbf{X}|\mathbf{X} \succeq \mathbf{0}_{L,R}\}$. Moreover, L_{m_k} is a bound on the Lipschitz constant of $\nabla_{\tilde{\mathbf{M}}}\mathcal{J}(\mathbf{m}_k, \mathbf{A}_k, \mathbf{W}_k, \mathbf{E}_k)$.

Algorithm 1: PNMM unmixing: global algorithm

Data: $\mathbf{Y}$

Input: $\mathbf{A}^0$, $\mathbf{M}^0$, $\underline{\mathbf{B}}^0$, $\boldsymbol{\alpha}^0$

$\mathbf{A} \leftarrow \mathbf{A}^0$

$\mathbf{M} \leftarrow \mathbf{M}^0$

$\underline{\mathbf{B}} \leftarrow \underline{\mathbf{B}}^0$

$\boldsymbol{\alpha} \leftarrow \boldsymbol{\alpha}^0$

while *stopping criterion not satisfied* **do**

  $\mathbf{M} \leftarrow \mathcal{P}_+\left(\mathbf{M} - \frac{\gamma}{L_M}\nabla_{\mathbf{M}}\mathcal{J}(\mathbf{M}, \mathbf{A}, \underline{\mathbf{B}}, \boldsymbol{\alpha})\right)$

  $\mathbf{A} \leftarrow \mathcal{P}_{\mathcal{A}}\left(\mathbf{A} - \frac{\gamma}{L_A}\nabla_{\mathbf{A}}\mathcal{J}(\mathbf{M}, \mathbf{A}, \underline{\mathbf{B}}, \boldsymbol{\alpha})\right)$

  for $i \leftarrow 0$ **to** V **do**

    $\mathbf{B}_i \leftarrow \mathrm{prox}_{\frac{\lambda}{L_{B_i}}\|.\|_1}\left(\mathcal{P}_{\mathcal{B}}\left(\mathbf{B}_i - \frac{\gamma}{L_{B_i}}\nabla_{\mathbf{B}_i}\mathcal{J}(\mathbf{M}, \mathbf{A}, \underline{\mathbf{B}}, \boldsymbol{\alpha})\right)\right)$

  for $i \leftarrow 1$ **to** V **do**

    for $k \leftarrow 1$ **to** K **do**

      $\alpha_{ki} \leftarrow \mathcal{P}_{\mathcal{R}}\left(\alpha_{ki} - \frac{\gamma}{L_{\alpha_{ki}}}\nabla_{\alpha_{ki}}\mathcal{J}(\mathbf{M}, \mathbf{A}, \underline{\mathbf{B}}, \boldsymbol{\alpha})\right)$

Result: $\mathbf{A}$, $\mathbf{M}$, $\underline{\mathbf{B}}$, $\boldsymbol{\alpha}$

3.3.2. Optimization with respect to $\mathbf{A}$

Similarly to paragraph 3.3.1, the abundance update is defined as the following

$$\mathbf{A} = \mathcal{P}_{\mathcal{A}}\left(\mathbf{A} - \frac{\gamma}{L_A}\nabla_{\mathbf{A}}\mathcal{J}(\mathbf{M}, \mathbf{A}, \underline{\mathbf{B}}, \boldsymbol{\alpha})\right) \tag{21}$$

where $\mathcal{P}_{\mathcal{A}}(\cdot)$ is the projection on the set $\mathcal{A}$ defined by the abundance constraints (4), which can be computed with efficient algorithms (see, e.g., the strategies discussed by Condat (2015)). Likewise, $L_{\tilde{A}}$ is the Lipschitz constant of $\nabla_{\tilde{A}}\mathcal{J}(\tilde{\mathbf{M}}, \tilde{\mathbf{A}}, \mathbf{Q}, \underline{\mathbf{B}})$.

3.3.3. Optimization with respect to $\mathbf{B}_i$

The updating rule for the basis function coefficients, under the constraints defined by (15), can be written as

$$\mathbf{B}_i = \text{prox}_{\frac{\lambda}{L_{B_i}}\|.\|_1}\left(\mathcal{P}_{\mathcal{B}}\left(\mathbf{B}_i - \frac{\gamma}{L_{B_i}}\nabla_{\mathbf{B}_i}\mathcal{J}(\mathbf{M}, \mathbf{A}, \underline{\mathbf{B}}, \boldsymbol{\alpha})\right)\right),$$

where $\mathcal{P}_{\mathcal{B}}$ is the projection into the set $\mathcal{B}$ defined by (15). Indeed, the proximal map of the sum of an indicator function and the ℓ_1-norm is exactly the composition of the proximal maps of both individual functions, following the same principle shown by Bolte et al. (2013). L_{B_i} is the Lipschitz constant of $\nabla_{B_i}\mathcal{J}(\tilde{\mathbf{A}}, \mathbf{B}, \mathbf{Q})$.

3.3.4. Optimization with respect to α_{ki}

Finally, the updating rule for the basis function exponential coefficients, under the constraints in (14), is

$$\alpha_{ki} = \mathcal{P}_{\mathcal{R}}\left(\alpha_{ki} - \frac{\gamma}{L_{\alpha_{ki}}}\nabla_{\alpha_{ki}}\mathcal{J}(\mathbf{M}, \mathbf{A}, \underline{\mathbf{B}}, \boldsymbol{\alpha})\right). \tag{22}$$

Also, $\mathcal{P}_{\mathcal{R}}$ is the projection into the set $\mathcal{R}$ defined in (14). The Lipschitz constant is $L_{\alpha_{ki}}$.

4. Evaluation on synthetic data

4.1. Synthetic data generation

To illustrate the accuracy of our algorithm, experiments are conducted on one $128 \times 128 \times 64$-pixel synthetic image with $L = 27$ times of acquisition ranging

from 1 to 15 minutes for a total period of 90 minutes. In this image, each voxel is constructed as a combination of $K = 3$ pure classes representative of the brain[1], which is the organ of interest in the present work: pure nSB gray matter, pure nSB white matter and pure blood or veins. Moreover, SB TACs are a result of nonlinearities affecting the pure nSB factors and, therefore, they do not represent new factors. The image is generated from the high resolution dynamic PET numerical phantom by Zubal et al. (1994) with TACs extracted from real PET images acquired with the Siemens HRRT and injected with ^{11}C-PE2I. In this extraction process, the ROIs of the real PET image were identified by segmenting a magnetic resonance image (MRI) to provide averaged TACs for each different tissue of the brain. The extracted TACs are not corrected for the decay of the isotope. The overall generation process is described in what follows:

- The dynamic PET phantom has been first linearly unmixed using the N-FINDR (Winter, 1999) and SUnSAL (Bioucas-Dias and Figueiredo, 2010) algorithms with an initial number of classes of 4, accounting for SB and nSB gray matter, white matter and blood. The TAC factor for SB gray matter found by N-FINDR is discarded while the other factors are selected to constitute the ground-truth non-specific factor TACs $\mathbf{m}_1, ..., \mathbf{m}_K$. The 4 factor proportions found by SUnSAL are used to generate 4 binary maps after a thresholding.

- The binary maps of SB and nSB gray matter generated from the SUnSAL output are merged to yield a general gray matter factor proportion. The white matter and blood binary maps are directly used as factor proportions. The final 3 binary maps are shown in the second row of Fig. 3.

- The SB gray matter binary map is used to provide the location of the weight coefficients of nonlinearity in the gray matter. An anomaly binary

[1]The choice of this number K of classes is further discussed in Section 6.

map is generated inside the white matter factor proportion to provide the location of SB in white matter.

- The weights and exponential coefficients describing the nonlinearities are generated from the full reference tissue model by Blomqvist et al. (1989), using equations from Lammertsma and Hume (1996), as reformulated in Häggström et al. (2016), where the exchange rate between compartments are subject to rate constants k_j with $j = 1, \cdots, 4$ (see Appendix A for more details on the link between these rate constants and the model parameters). More precisely, to identify a relevant range of values for the kinetic parameters, the initial SB TAC has been approximated with the previously mentioned compartment model. Then, these kinetic parameters are slightly perturbed to produce several SB TACs for different regions of the brain, in agreement with the slight variations that could be observed with DEPICT Gunn et al. (2002). Moreover, two overall levels of binding are generated for each tissue by altering the tracer delivery ratios R_{1n} $(n = 1, \ldots, N)$ between the tissue of interest and the reference tissue. More precisely, for the SB gray matter, the tracer delivery ratios R_{1n} take values in $\{1, 1.6\}$ according to a spatially coherent pattern, i.e., the same R_{1n} is set to each pixel inside a non-zero uniform area of the binary map. The other parameters are set to $k_2 = 0.4$, $k_3 = 0.15$ and $k_4 = 0.01$ for all non-zero pixels of the binary map. For the SB white matter, similarly the parameters are set to $R_{1n} \in \{1, 1.6\}$, $k_2 = 0.3$, $k_3 = 0.15$ and $k_4 = 0.01$.

- Parameter generation directly yields the exponential coefficients $\boldsymbol{\alpha}_1, \cdots, \boldsymbol{\alpha}_V$, while the computed weights are inserted in place of the non-zero values of the previously defined SB binary maps for the gray and white matters, accordingly. The binding potentials denoted $\mathrm{BP}_{\mathrm{ND_G}}$ and $\mathrm{BP}_{\mathrm{ND_W}}$ computed following (7) for the gray and white matters, respectively, are shown in Fig. 1.

After the phantom generation process, a PSF defined as a space-invariant and isotropic Gaussian filter with FWHM = 4.4mm is applied to the output

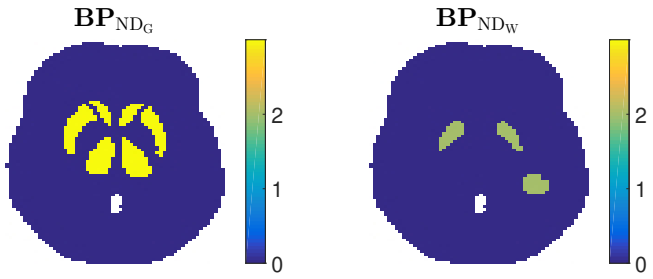

Figure 1: Binding potential maps w.r.t. the nondisplaceable radioligand in tissue. The gray matter binary map represents the striatum, which absorbs ^{11}C-PE2I even in healthy controls (see Emond et al. (2008)), and the thalamus which was added for a broader area. The white matter binary map is composed by part of the striatum for demonstration purposes and by an artificial circular anomaly.

image. Finally, as proposed by Cavalcanti et al. (2018), the measurements are corrupted by a Gaussian noise with a signal-to-noise ratio (SNR) of 20dB. For illustration purpose, Fig. 2 depicts some resulting noisy TACs associated with gray and white matters. Simulations were conducted with 20 different noise realizations to get statistically reliable performance measures. For sake of fair comparison, the ground-truth for the factor proportions $\mathbf{A}$ (first row of Fig. 3) and the basis function coefficients $\underline{\mathbf{B}}$ corresponding to nonlinearities are computed by applying the proposed algorithm with fixed factors and exponential coefficients, i.e., by updating only the two variables of interest, in a noise-free image convolved with the PSF. This allows the PVE to be taken into account.

4.2. Compared methods

The proposed PNMM unmixing technique is compared against the basis pursuit method by Gunn et al. (2002), referred to as DEPICT, and the specific binding linear mixing model (SLMM) unmixing we already proposed (Cavalcanti et al., 2018). Their implementations are detailed in what follows.

DEPICT – In this work, DEPICT is implemented with proximal gradient steps for comparison purposes. As proposed by Gunn et al. (2002), basis pursuit denoising is conducted with 30 basis functions logarithmically spaced between

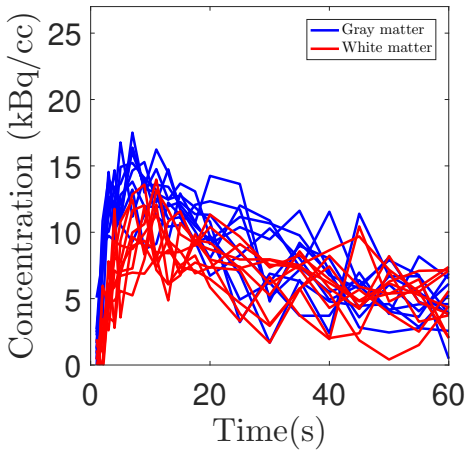

Figure 2: Some synthetic TACs for gray and white matters.

the decay constant (which is 0.034 min^{-1}) and 6 min^{-1} and an additional basis function to represent the offset. Note that the decay constant is used as one of the basis functions in the simulated experiment because the image has not been corrected w.r.t. the decay of the isotope in this case (Gunn et al., 2002). The number of basis functions is fixed to 31 as a trade-off between precision and computation time. For comparison purposes, DEPICT is conducted with two different reference TACs: first the gray, then the white matter factors that are defined as described in the following PNMM-unmixing dedicated paragraph (see below).

SLMM-unmixing – To appreciate the interest of extracting a physically interpretable quantity, the proposed algorithm is also compared with the previous method introduced by Cavalcanti et al. (2018). This SLMM method considers an additional class dedicated to SB. The penalizations chosen for $\mathbf{M}$ and $\mathbf{A}$ are the same, as the one for matrix $\mathbf{B}$ in SLMM and the set of matrices $\underline{\mathbf{B}}$ in PNMM. Thus, we consider the same regularization parameters (see Table 1) for fair comparisons. The algorithm is stopped when the normalized difference between two consecutive objective function values is below a threshold ε set to 5×10^{-3}. The variability dictionary is learned from a predefined high-uptake

region of the image, comprising both SB gray and white matters. Blood, white matter and gray matter factors and their corresponding proportions are initialized as described in the next paragraph dedicated to PNMM (see below). The factor and factor proportion related to SB are initialized with zeros, as is the matrix $\mathbf{B}$. We allow the method to run 50 iterations with fixed $\mathbf{M}$ so as to improve the initializations of $\mathbf{A}$ and $\mathbf{B}$, while preventing factors from merging.

PNMM-unmixing – For the proposed algorithm, factor proportions are initialized with the binary maps coming from the generation process. In a real applicative context, this would be equivalent to using an MRI segmentation to produce the maps of tissues. Regarding the initialization of the factors, the TACs from each tissue are organized from the lowest area-under the curve (AUC) TAC to the highest. The first 10% AUC TACs are discarded and we average the TACs whose AUC are the 10% to 20% lowest ones. Then, the basis functions and their corresponding coefficients are computed with an instance of our algorithm, where factors and proportion maps are not updated. As suggested by Gunn et al. (2002), since the image has not been corrected w.r.t. the decay of the isotope, the exponential coefficients are bounded with $\alpha_i^{\min} = d_c$ $(\forall i)$, where $d_c = 0.034$ min^{-1} is the decay constant for $[11C]$, and $\alpha_i^{\max} = 6$ min^{-1}. Limits are also imposed for the nonlinearity coefficients. Because of the model configuration in PNMM, which uses different inputs for gray and white matters, $b_{0n} = R_{1n} - 1$ is expected to be nonnegative in SB tissues when nSB tissues are used as a reference if the blood flow within each tissue is homogeneous in all areas, which is the assumption here. Moreover, following this assumption, the maximum value of R_{1n} is not expected to be higher than 1.7. Thus, the extremal values of the admissible sets are chosen as $b_0^{\min} = 0$ and $b_0^{\max} = 0.7$. The limits for the nonlinearity coefficients can be chosen by analyzing the relations of the known kinetic parameters of the tracer under study and the weights. In the conducted study, it appears sufficient to choose $b_1^{\min} = -0.2$, $b_1^{\max} = 0$, $b_2^{\min} = 0$ and $b_2^{\max} = 0.15$. Table 1 summarizes the sets of admissible values of the kinetic parameters and the regularization parameters.

Table 1: Model parameters and limits

	Synthetic data		Real data	
	PNMM	SLMM	PNMM	SLMM
η	0.500	0.500	0.035	0.035
β	0.100	0.100	0.001	0.001
λ	0.500	0.500	0.02	0.02
$\alpha_i^{\min}$	0.034	-	0.01	-
$\alpha_i^{\max}$	6	-	6	-
$\mathbf{b}^{\min}$	[0, -0.2, 0]	-	[-1, -1, -1]	-
$\mathbf{b}^{\max}$	[0.7, 0, 0.15]	-	[1, 1, 1]	-

4.3. Figures-of-merit

4.3.1. Normalized mean squared error

The performance of the method is measured by computing the normalized mean square error (NMSE)

$$\text{NMSE}(\hat{\boldsymbol{\theta}}) = \frac{\|\hat{\boldsymbol{\theta}} - \boldsymbol{\theta}^*\|_{\text{F}}^2}{\|\boldsymbol{\theta}^*\|_{\text{F}}^2}, \tag{23}$$

where $\boldsymbol{\theta}^*$ and $\hat{\boldsymbol{\theta}}$ are the true and estimated latent variables, respectively. This metric is evaluated for the following variables: the factor proportions $\mathbf{A}$, the non-specific factor TACs $\mathbf{M}$, the tracer delivery ratio $\mathbf{R}_1 = [R_{11}, \ldots, R_{1N}]^T$, the kinetic parameter $\boldsymbol{\alpha}$, the overall binding potentials $\mathbf{BP}_{\text{ND}}$ w.r.t. the nondisplaceable radioligand in tissue as well as the individual potentials $\text{BP}_{\text{ND}_\text{G}}$ and $\text{BP}_{\text{ND}_\text{W}}$ associated with the gray and white matters, respectively.

4.3.2. Average Mean Absolute Percentage Error

To obtain a measure more robust w.r.t. possible outliers, the mean absolute percentage error (MAPE) is also considered as a figure-of-merit. For a d-dimensional latent variable $\boldsymbol{\theta} = [\theta_1, \ldots, \theta_d]$, the average MAPE (aMAPE) is defined as

$$\text{aMAPE}(\hat{\boldsymbol{\theta}}) = \frac{1}{d}\sum_{i=1}^{d}\left|\frac{\hat{\theta}_i - \theta_i^*}{\theta_i^* + \epsilon}\right|, \tag{24}$$

where $\boldsymbol{\theta}_i^*$ and $\hat{\boldsymbol{\theta}}_i$ are the true and estimated latent variables, respectively. The constant ϵ, chosen as 10% of the maximum value of each analyzed variable, is introduced to prevent numerical instabilities when ground truth values are close to zero. The aMAPE is considered as a performance measure for the estimations of the same quantities of interest as for NMSE.

4.4. Results

Fig. 3 shows, from top to bottom: the ground-truth factor proportion, the initial segmentation and the final SLMM and PNMM results. The first column shows the gray matter, the second column shows the white matter and the third column presents the blood factor proportion. Visual analysis suggests that both SLMM and PNMM techniques are able to include the PVE into the factor proportions, as expected. Note that the SB gray and white matters do not appear on the corresponding SLMM factor proportion, since the algorithm deals with nSB and SB as different tissues.

The estimated nSB gray and white matter factors are displayed in Fig. 4, together with their initialization. Visual comparison suggests that PNMM improves the initial factor estimation with final global TACs that are very close to the ground-truth. Comparatively, the SLMM result for the blood TAC is clearly less accurate.

These results are further confirmed by the quantitative evaluation of Table 2 that shows the NMSE and aMAPE of the variables of interest as estimated during the initialization and after conducting SLMM and PNMM unmixing for the 20 noise realizations. As SLMM is supposed to identify the SB regions with an exclusive factor, it would be quite unfair to crudely interpret that its estimated abundance maps is poor, since this initialization framework is not ideal for SLMM.

The PNMM results for both $\mathbf{A}$ and $\mathbf{M}$ are remarkably improved. This is a favorable outcome, since it suggests that PNMM is able to improve the results with this initialization setting that can be easily replicated in real image applications.

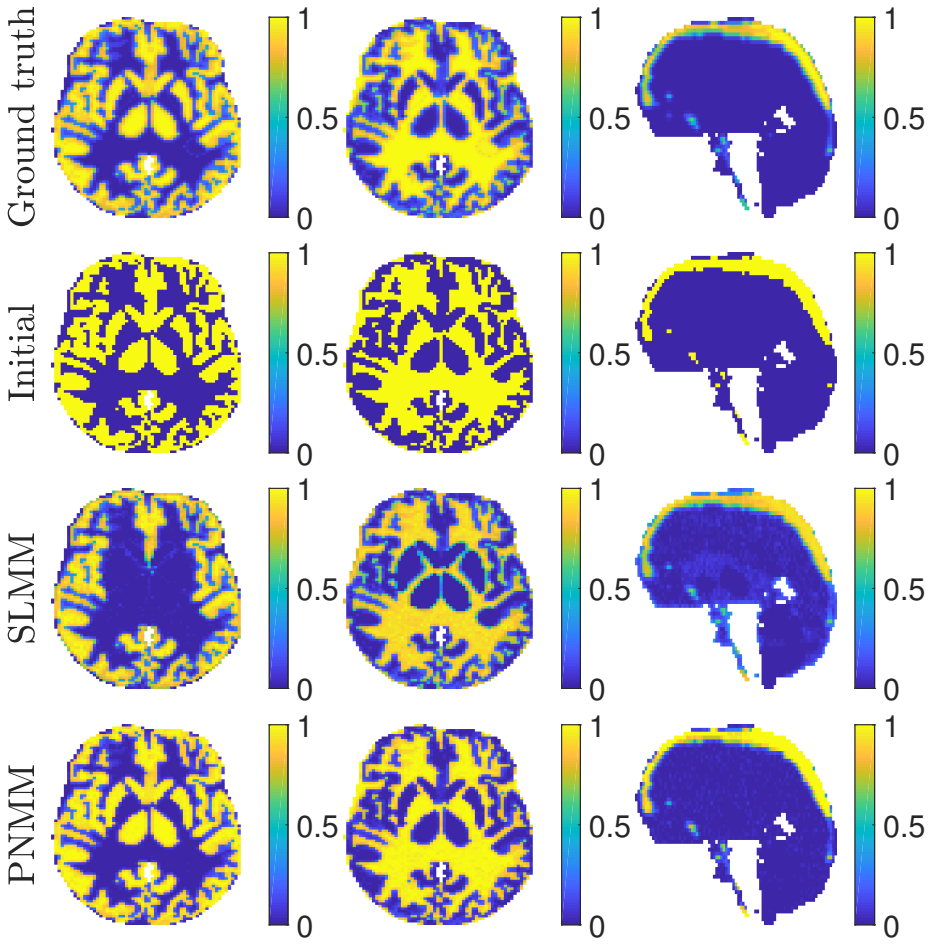

Figure 3: Factor proportion maps obtained from the synthetic image corresponding to the gray matter, white matter and blood, from left to right. The first 2 columns show transaxial views while the last one shows a sagittal view. All images are in the same scale $[0, 1]$. Both algorithms are able to take the PVE into account. SB regions are not present in the SLMM maps, as the algorithm deals with SB as a separate TAC.

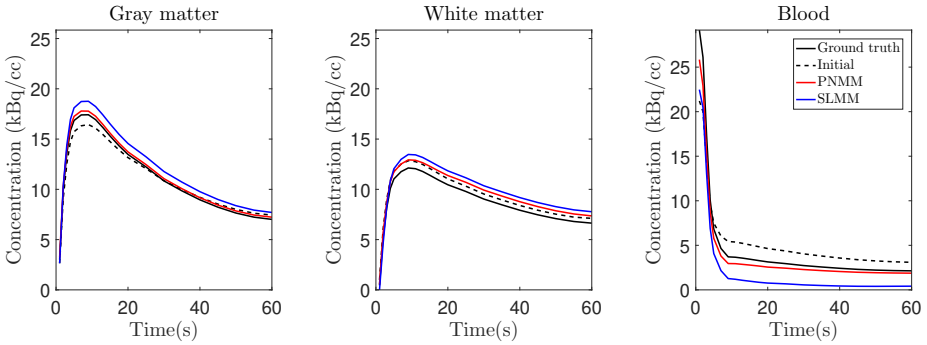

Figure 4: Factor TACs estimated from the synthetic image. PNMM produces final TACs that are very close to the ground-truth.

Table 2: Mean and standard deviation of both NMSE and aMAPE for $\mathbf{A}$, $\mathbf{M}$, $\mathbf{R}_1$, $\boldsymbol{\alpha}$ and $\mathbf{BP}$ as chosen in initialization and after conducting PNMM-unmixing over 20 noise realizations.

	NMSE			aMAPE		
	Init.	PNMM	SLMM	Init.	PNMM	SLMM
$\mathbf{A}$	0.236 $\pm 1 \times 10^{-5}$	0.101 $\pm 4 \times 10^{-6}$	0.421 $\pm 1 \times 10^{-5}$	0.179 $\pm 3 \times 10^{-33}$	0.108 $\pm 8 \times 10^{-6}$	0.468 $\pm 3 \times 10^{-5}$
$\mathbf{M}$	0.165 $\pm 4 \times 10^{-8}$	0.136 $\pm 5 \times 10^{-7}$	0.182 $\pm 5 \times 10^{-7}$	0.090 $\pm 8 \times 10^{-8}$	0.059 $\pm 7 \times 10^{-7}$	0.126 $\pm 6 \times 10^{-7}$
$\mathbf{R}_1$	1.304 $\pm 1 \times 10^{-4}$	0.601 $\pm 1 \times 10^{-5}$	-	0.506 $\pm 3 \times 10^{-5}$	0.117 $\pm 3 \times 10^{-5}$	-
$\boldsymbol{\alpha}$	0.210 $\pm 6 \times 10^{-10}$	0.204 $\pm 5 \times 10^{-8}$	-	0.094 $\pm 1 \times 10^{-10}$	0.091 $\pm 1 \times 10^{-8}$	-
$\mathrm{BP_{ND}}$	0.156 $\pm 1 \times 10^{-7}$	0.097 $\pm 8 \times 10^{-8}$	-	0.072 $\pm 1 \times 10^{-7}$	0.052 $\pm 4 \times 10^{-8}$	-
$\mathrm{BP_{ND_G}}$	0.170 $\pm 4 \times 10^{-7}$	0.183 $\pm 6 \times 10^{-7}$	-	0.068 $\pm 4 \times 10^{-7}$	0.079 $\pm 2 \times 10^{-7}$	-
$\mathrm{BP_{ND_W}}$	0.153 $\pm 1 \times 10^{-7}$	0.071 $\pm 2 \times 10^{-7}$	-	0.088 $\pm 2 \times 10^{-7}$	0.039 $\pm 2 \times 10^{-8}$	-

Fig. 5 shows the binding potential w.r.t. the nondisplaceable radioligand in tissue $\mathbf{BP}_{\mathrm{ND}}$ for the gray matter (left) and white matter (right). The first two rows present the ground-truth and initial $\mathbf{BP}_{\mathrm{ND}}$ and the last row presents the PNMM estimation of $\mathbf{BP}_{\mathrm{ND}}$ in the PNMM formulation, where there are two $\mathbf{BP}_{\mathrm{ND}}$ to be estimated in the same setting: one for the gray matter ($\mathbf{BP}_{\mathrm{ND_G}}$) and one for the white matter ($\mathbf{BP}_{\mathrm{ND_W}}$). It is hard to determine by visual comparison whether the binding potential is improved from initialization by the PNMM-unmixing. Table 2 presents the quantitative results of the NMSE and aMAPE for the matrix $\mathbf{R}_1$, where the estimated $\mathbf{b}_{0n}$ includes the coefficients for both non-specific tissues, and the NMSE and MAPE for the matrix $\mathbf{BP}_{\mathrm{ND}}$ with the binding potential in each voxel for each tissue. Quantitative results suggest that $\mathbf{BP}_{\mathrm{ND_G}}$ is slightly less well estimated by PNMM-unmixing, while $\mathbf{BP}_{\mathrm{ND_W}}$ is much better estimated by conducting the whole PNMM-unmixing, which is natural since the estimations of the factors and factor proportions are also improved. Moreover, the ratio of delivery of the tracer $\mathbf{R}_1$ seems to show a much greater improvement.

Moreover, for comparison, Fig. 6 reports the SLMM results for the factor proportion and the internal variability (left column) and the DEPICT results taking the white matter as reference TAC, denoted by $\mathrm{BP}_{\mathrm{ND}_{Ref:\mathrm{W}}}$ and the gray matter as reference TAC, denoted by $\mathrm{BP}_{\mathrm{ND}_{Ref:\mathrm{G}}}$ (right column). SLMM results are not equivalent to the binding potential or any other physical quantity of clinical use. Still, it is possible to see that SB tissues have been identified and the missing regions from gray and white matter factor proportions of Fig. 3 are relocated in the SB factor proportion. The evaluation of $\mathbf{R}_1$ and $\mathrm{BP}_{\mathrm{ND}}$ cannot be conducted for the DEPICT result, since the ground-truths are not equivalent. Visual inspection suggests that DEPICT is able to correctly locate the SB tissues with similar intensities of $\mathrm{BP}_{\mathrm{ND}}$. The gray matter result presents some binding in the white matter tissue, showing the potential bias that could be expected when the whole image is represented by one reference TAC, while considering distinct reference TACs in distinct nSB tissues seems more accurate. Even though the overall result may often be sufficient for clinical applications,

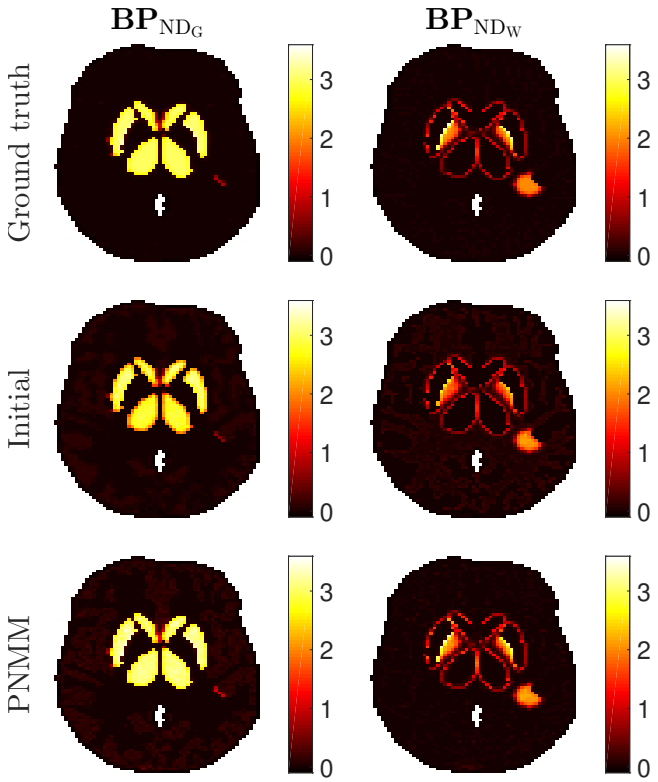

Figure 5: From top to bottom: ground-truth, initial and PNMM estimations of $\mathbf{BP}_{\mathrm{ND}}$. The first column corresponds to the gray matter and the second to the white matter. Both the initialization with compartmental modeling and PNMM are able to correctly identify the areas affected by SB but the small differences of precision (as a little noise in the initialization map) are more clearly perceived on numerical comparisons.

given the challenge of interpreting dynamic PET images, they seem to be less accurate than the method herein proposed, in terms of both BP intensities and location. Moreover, DEPICT does not allow the user to differentiate the tissue that is affected, for instance, by an abnormality, while our method may provide this detailed information.

Note that if the factor proportions are initialized and fixed based on an MRI segmentation, PNMM works as a local reference model, where each non-specific tissue of the image is treated as a different ROI and is therefore allowed to have its own reference TAC. This is equivalent of conducting DEPICT in each

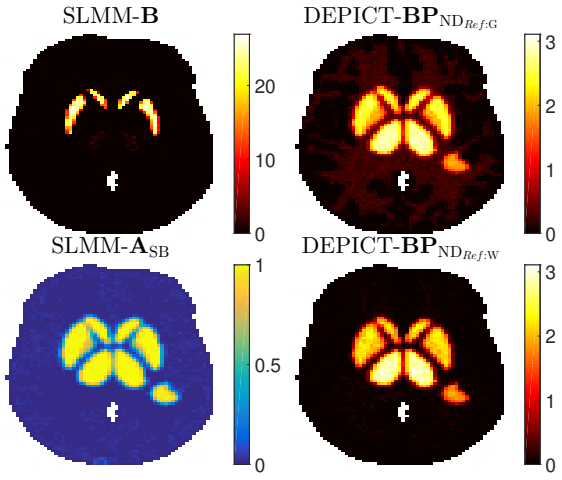

Figure 6: The left column shows SLMM variability result (top) and SLMM factor proportion related to the SB TAC (bottom) and the right column shows DEPICT BP_{ND} estimation using the gray (top) and white (bottom) matters as reference TACs, respectively. Note that DEPICT BP_{ND} was estimated for the whole image using the respective tissue TAC as reference. SLMM is able to correctly identify the areas affected by SB but, differently from DEPICT, its result does not present a physical meaning.

segmented tissue, but allowing the global reference TAC to be improved in each step. This setting is also able to provide the tissues affected by SB but does not take into account the PVE.

5. Evaluation on real data

5.1. PET data acquisition

To assess the performance of the proposed approach on a real dataset, the compared methods have been applied to a dynamic PET image acquired with an Ingenuity TOF Camera from Philips Medical Systems of a stroke subject injected with [18F]DPA-714, seven days after the stroke. The PET acquisition was reconstructed into a $128 \times 128 \times 90$-voxels dynamic PET image with $L = 31$ time-frames. The PET scan image registration time ranged from 10 seconds to 5 minutes over a 59 minutes period. The voxel size was of $2 \times 2 \times 2$ mm^3.

5.2. Compared methods

Factor proportions are initialized with binary maps mainly constituted from a manually labelled MRI segmentation and improved with a K-means for the voxels that were not labelled in the MRI segmentation. Note that other types of initialization that might be useful in such a case include SuperVised Cluster Analysis (SVCA) (Boellaard et al. (2008)), an atlas-based segmentation, population-based classes or even K-means also for the tissues with a visual check of the provided final TACs and regions. Factors are initialized as in the synthetic case. The stroke region is identified from the segmentation of this registered MRI image. It is used to define a set of voxels used to learn the spatial variability descriptors for SLMM-unmixing. The nominal SB TAC for SLMM is fixed as the empirical average of the corresponding TACs with AUC comprised between the 10th and 20th percentile. The matrix $\mathbf{B}$ is initialized with zeros and, as before, we allow the method to run 50 iterations with fixed $\mathbf{M}$.

As the image has been previously corrected w.r.t. the decay of the isotope, the tracer decay cannot be longer included as one of the basis functions, as done in the synthetic case (see Section 4). Instead, a set of 30 values have been generated as logarithmically spaced between 0.206 and 6 min^{-1} (see Appendix F for details). Then, an additional basis function is added to represent the offset.

For PNMM, the basis functions and their corresponding coefficients are initialized as in the synthetic case, with an instance of our algorithm, where factors and proportion maps are not updated. The exponential coefficients are constrained according to (14) with $\alpha^{\min} = 0.05\ \text{min}^{-1}$ and $\alpha^{\max} = 6\ \text{min}^{-1}$. The nonlinearity coefficients are constrained following (15) with $b_i^{\min} = -1$ (since blood flow homogeneity cannot be assumed) and $b_i^{\max} = 1$ ($i = 0, \ldots, V$). Table 1 summarized the choice of the admissible ranges for the kinetic parameters and the values of the model parameters.

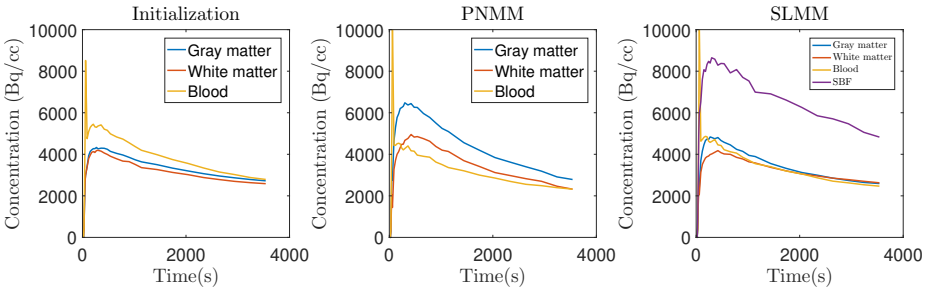

Figure 7: Factor TACs estimated from the real image. PNMM is able to recover more realistic TACs for gray and white matters and for the blood, performing better than SLMM and improving the initialization.

5.3. Results

Fig. 7 presents the initial and estimated factor TACs. The initial gray and white matter factor TACs are very similar. SLMM is able to separate the gray and white matter factor TACs but they still present lower AUCs than the blood TAC, which is not expected in reality. This may be because the SB TAC, which is fixed, is very close to the gray matter factor TAC, inducing the gray matter factor to be smaller. On the other hand, PNMM is able to differentiate the gray and white matter factor TACs in both intensity and shape. It is also able to estimate a more realistic blood factor with decreased AUC, which is expected since the blood is supposed to present a peak of concentration at the moment of radiotracer injection and then reduce the concentration over time. This improvement on the tissue TACs is very relevant since it will have a direct impact on subsequent computations of the binding potentials.

Fig. 8 shows a 3D visualization of the initialization and PNMM results corresponding to the different tissues, i.e., from top to bottom, the initialized gray matter factor proportion, the gray matter factor proportion recovered by PNMM, the gray matter binding potential recovered by PNMM, the initialized white matter factor proportion, the white matter factor proportion recovered by PNMM and the white matter binding potential recovered PNMM. The gray and white matter binding potentials as well as factor proportions seem

complementary, i.e., the SB regions missing in the PNMM binding potential for the gray matter can be found in the result for the white matter and the same is valid for the factor proportions. Note that the binding potential $\mathbf{BP}_{\mathrm{ND}}$ for each tissue matches the corresponding factor proportion as a consequence of the mathematical formulation of the problem. This result highlights the fact that the algorithm is not only able to correctly locate the region affected by the stroke, but is also able to identify the affected tissues.

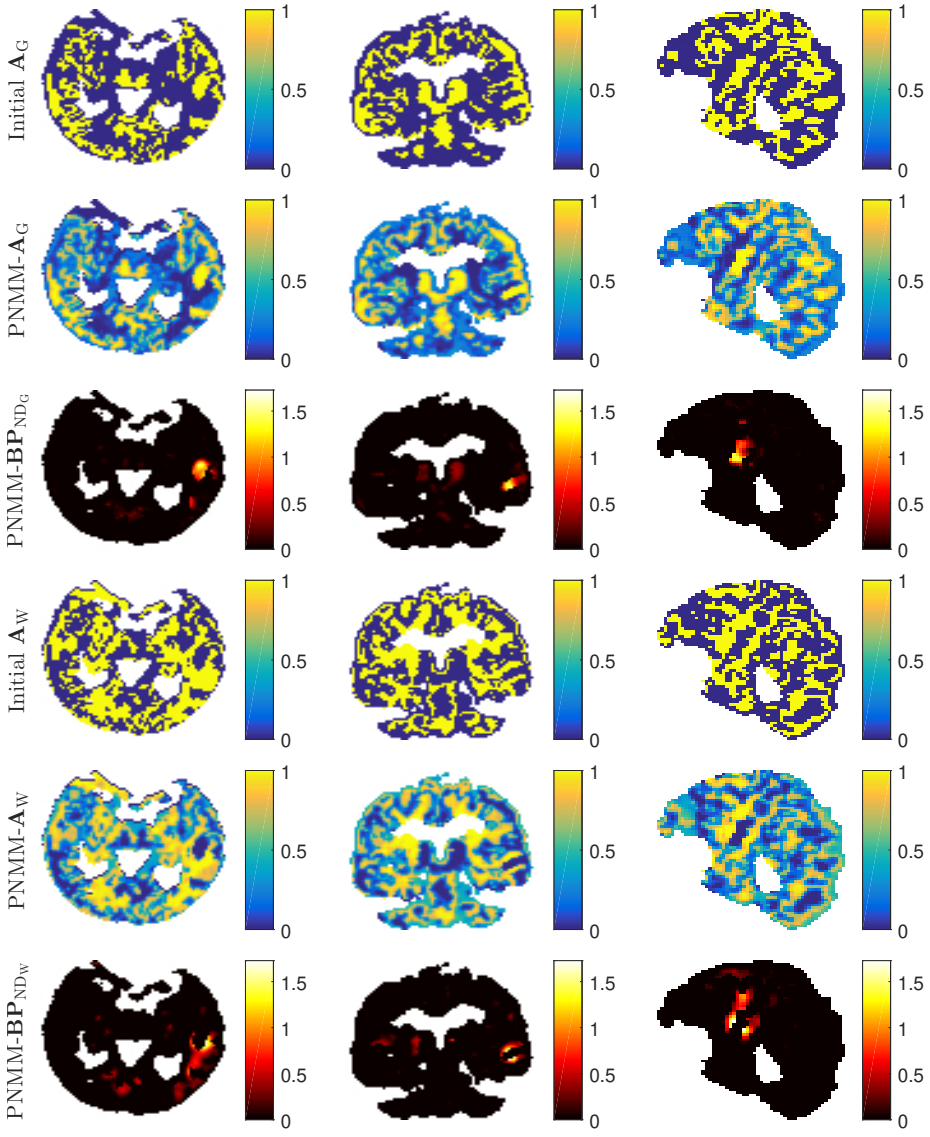

Figure 8: From top to bottom: initialized gray matter factor proportion, the gray matter factor proportion recovered by PNMM, the gray matter binding potential recovered by PNMM, the initialized white matter factor proportion, the white matter factor proportion recovered by PNMM and the white matter binding potential recovered PNMM. From left to right: transaxial, coronal and sagittal views. The gray and white matter factor proportions and $\mathbf{BP}_{\mathrm{ND}}$ maps recovered by PNMM are complementary.

Fig. 9 shows a 3D visualization of the SB region, i.e., from top to bottom, the

stroke identified by MRI segmentation, the binding potentials $\mathrm{BP}_{\mathrm{ND}_{Ref:\mathrm{W}}}$ and $\mathrm{BP}_{\mathrm{ND}_{Ref:\mathrm{G}}}$ recovered by DEPICT using the initial white and gray matter TAC as references, respectively, and the overall binding potential $\mathbf{BP}_{\mathrm{ND}_{\mathrm{G+W}}}$ recovered by PNMM computed as the weighted sum of $\mathbf{BP}_{\mathrm{ND}_{\mathrm{G}}}$ and $\mathbf{BP}_{\mathrm{ND}_{\mathrm{W}}}$ to provide a comprehensive representation of the stroke region[2]. Visual inspection suggests that DEPICT presents high **BP** intensities in brain regions not expected to be affected by SB as well as a binding potential that ranges from 0 to 4, higher than the one found by PNMM. This is due to the fact that the AUC from the tissue TACs provided in the initialization step are lower than the ones found by PNMM. Thus the differences have to be mitigated by the binding potential. Conversely, PNMM seems visually more accurate, capturing with precision the stroke region and provides a binding potential that ranges from 0 to 2. This is due to the simultaneous update of the factors, that improves the initialization step, as seen in Fig. 7. This means that, even when providing a poor TAC initialization, the proposed method is able to recover a relevant estimation of the binding potential, while other methods are highly dependent on the quality of the provided tissue TAC.

While DEPICT provides the binding potential for the entire image, the PNMM result is able to provide the SB voxels for each tissue. In addition, by combining the results per tissue, we are able to acquire a complete vision of the binding potential. To summarize, it seems that PNMM is able to locate the SB in the entire image as soon as the results associated with the different tissues are combined. Compared to DEPICT, the PNMM results seem more accurate, partly because exploiting the same reference TAC in DEPICT is expected to bias the analysis.

[2]The choice of the weighted sum as a summary quantity is further discussed and compared to other choices in Section 6.

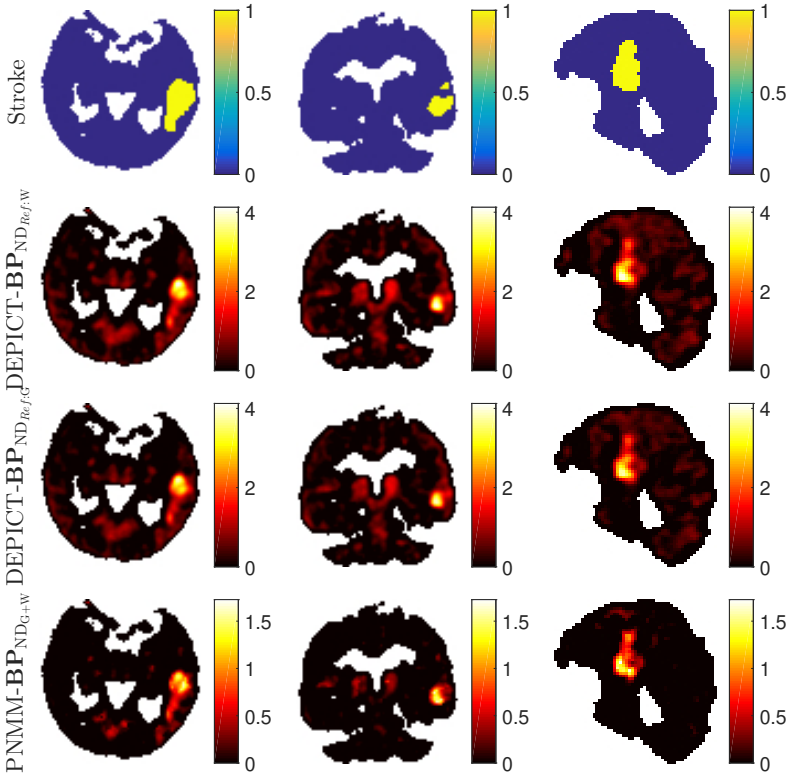

Figure 9: From top to bottom: stroke region identified by MRI segmentation, the binding potentials $\mathbf{BP}_{\mathrm{ND}_{Ref:\mathrm{W}}}$ and $\mathbf{BP}_{\mathrm{ND}_{Ref:\mathrm{G}}}$ recovered by DEPICT using the initial white and gray matter TAC as references, respectively, and the binding potential $\mathbf{BP}_{\mathrm{ND}_{\mathrm{G+W}}}$ recovered by PNMM. From left to right: transaxial, coronal and sagittal views. The PNMM result corresponds to the weighted sum of $\mathbf{BP}_{\mathrm{ND}_{\mathrm{G}}}$ and $\mathbf{BP}_{\mathrm{ND}_{\mathrm{W}}}$ and it is actually much more localized in the SB regions than DEPICT.

Finally, Fig. 10 shows the factor proportion $\mathbf{A}_{\mathrm{SB}}$ and internal variability $\mathbf{B}$ estimated by SLMM. The factor proportion presents a soft highlight on the SB area affected by the variability, which is a relevant outcome, especially because this factor proportion was initialized with zeros. However, it also includes part of the nSB gray matter as SB tissue, biasing the TACs. The variability $\mathbf{B}$, which is not a physically interpretable quantity, correctly identifies the SB area, which is complementary to the information brought by the corresponding factor

proportion. Although the result is informative, it is not complete in terms of clinical assessment, in opposition to the other two methods studied.

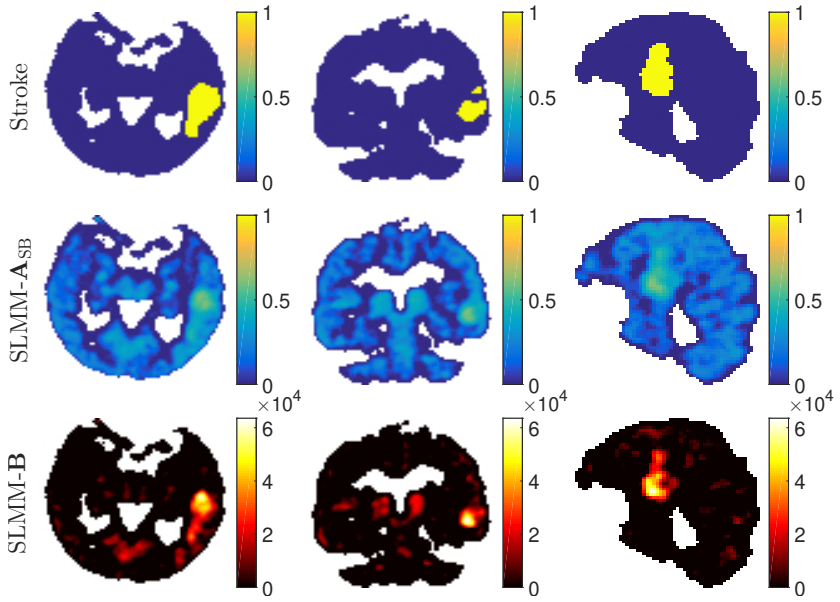

Figure 10: From top to bottom: stroke identified by MRI segmentation, SB factor proportion estimated by SLMM and internal variability estimated by SLMM. From left to right: transaxial, coronal and sagittal views. SLMM correctly identifies the SB area but the variability map values do not have a physical meaning.

6. Discussion

Combining factor analysis and compartmental modeling – Although compartmental models may appear to be complex, they have been widely advocated in the literature to analyze and interpret dynamic PET data. Similarly, factor analysis is also a very popular technique to extract TACs of reference and input functions that are then processed through those compartmental models. The nonlinear unmixing strategy derived in this paper is nothing more than combining these two widely used processing techniques into a unique framework. By tackling both problems jointly instead of

sequentially, the experiments conducted in Sections 4 and 5 show that this can improve the accuracy of the analysis. Despite the resulting seemingly complex model, it is worth noting that the proposed method does not involve more parameters than those separately estimated by conventional factor analysis followed by compartmental modeling.

Accounting for tissue heterogeneity – One of the main novelty of the PNMM method is its ability to account for differences in tissues properties. For instance, this is of particular interest when evaluating the effects of an intervention or a focal disease, such as the stroke considered in the experiments conducted in Section 5. In this context of brain imaging, the proposed method allows relative changes of the binding potential to be estimated between healthy and unhealthy tissues, in particular when the baseline potential is different between white and gray matters.

Factor analysis vs. PVE correction – The proposed method aims at recovering the ground truth parameters while accounting for PVE. However, *per se*, it should not be understood as a straight PVE correction approach. This is why the performance of the method has not been assessed with respect to this sole purpose in the experiments conducted in Sections 4 and 5. Besides, one of the main differences with the PVE correction method referred to as Iterative Yang (IY) (Yang et al., 1996; Erlandsson et al., 2012) is that the latter method builds a PVE correction based on anatomical information coming from MRI in addition to the PET data itself. This brings a substantial advantage when quantitative analysis is based on ROIs defined from the MRI data of the subject.

Regularizations and constraints – Due to the ill-posedness of the problem, the proposed factor model is complemented with suitable regularizations (i.e., prior information) to reach sound solutions. In the experiments conducted in Sections 4 and 5, SB is expected to affect a small area of the brain. As a consequence, a spatial sparsity-promoting regularization (i.e., based on the

$\ell_{2,1}$-norm) is considered for the internal coefficients $\underline{\mathbf{B}}$. Of course, in a different applicative context, the proposed approach should be adapted by designing an adequate regularization. For instance, for more diffuse expected SB, this could be a Sobolev norm to promote the spatial smoothness of the coefficients.

Moreover, following the DEPICT method that inspired the proposed compartmental modeling Gunn et al. (2002), the kinetic parameters for the synthetic data experiments have been assumed to be bounded with $\alpha_i^{\min} = d_c$ $(\forall i)$, where d_c is the decay constant of the tracer. This setting is only recommended for cases where the PET image has not been corrected for the decay of the isotope, which is the case for the synthetic data but not for the real data. Therefore, a different setting was specified for the latter with $\alpha_i^{\min}$ set to a value greater than the decay constant. More generally, within an estimation process following clinical trials, it is a common practice to assume that parameters have to satisfy specific constraints associated with a given acquisition protocol associated with particular radiotracer and pathology. In other words, for other tracers, the constraints imposed to the kinetic parameters should be adapted accordingly.

Number K of classes – In the experiments conducted in Section 4 and 4.4, the number of classes has been set to $K = 3$, which includes the gray matter, the white matter and the blood. Blood has been considered as a separate class since it is not affected by binding. An additional class associated with cerebrospinal fluid (CSF) could have been included into the proposed model. However, the rationale of the proposed method is rather to focus on the classes that are already considered by the SVCA approach and thus to handle partial volume effects (PVE) within the brain tissue. Moreover, including a CSF class would have increased significantly the complexity of the method with many extra parameters to be estimated, for a modest expected gain. As a consequence, to mitigate the influence of this additional class that could be induced by PVE, in the experiments reported in Section 5, the CSF and null areas have been discarded with a mask covering also

the neighboring pixels that may have been affected, as in Boellaard et al. (2008).

Summary visualization of $\mathbf{BP}_{\mathrm{ND}}$ – The analysis of the binding potentials per tissue offered by PNMM permits an insightful understanding of the effects of SB, as represented in Fig. 8. When a unique visualization is required for multiple tissues, e.g., for an application purpose, multiple maps of binding potential should be combined. In particular, for comparison with DEPICT results in Section 4.4, Fig. 9 depicts the weighted sum of the potentials associated with each tissue since it seems to be the most physically meaningful. Obviously, alternative choices can be adopted, such as the ordinary sum or the maximum. To illustrate, these three possibilities are depicted in Fig. 11. The results appear to be similar in this experiment.

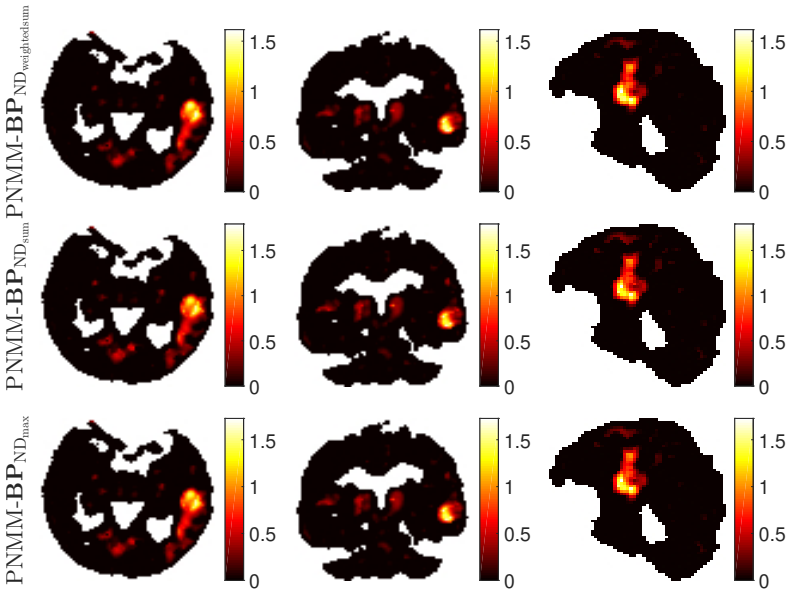

Figure 11: From top to bottom: weighted sum, ordinary sum and maximum as summary quantities of the overall binding potential recovered by PNMM. From left to right: transaxial, coronal and sagittal views.

7. Conclusion

This paper presented a novel technique for dynamic PET analysis that combined nonlinear unmixing and parametric imaging to yield a clinically interpretable result for factor analysis. To this end, this work was based on reference tissue input models with reversible kinetics to produce a physically meaningful nonlinearity affecting the TACs of nSB tissues. Moreover, it considered the mixed kinetics that can be present in each voxel due to partial volume, PSF and biological heterogeneity. The resulting method managed to recover the binding potential related to the different responses of the tissues to tracer kinetics on simulations. It also provided the tissue affected by abnormalities. The potential interest of this novel technique was evaluated on synthetic and real data, showing promising results. Future works should focus on generalizing this model for settings with irreversible kinetics.

Acknowledgments

The authors would like to thank Dr. Simon Stute, formerly with IMIV (UMR U1023 CEA-INSERM-CNRS, Univ. Paris-Saclay, France) and now with CRCINA (UMR U1232 INSERM-CNRS, Univ. Nantes, France) for providing the real TACs used to generate the synthetic images used in Section 4.

Appendix A. Full reference tissue compartment model

The full reference tissue compartment model (FRTM) of Häggström et al. (2016), whose compartmental structure is depicted in Fig. A.12 (Blomqvist et al., 1989; Cunningham et al., 1991; Lammertsma and Hume, 1996), makes use of a region of reference that is supposed to be devoid of the target of the radiotracer. According to this model, the PET signal writes

$$C_{\mathrm{T}} = R_1 C_{\mathrm{R}}(1 + b_1 * e^{-\alpha_1 \mathbf{t}} + b_2 * e^{-\alpha_2 \mathbf{t}}), \tag{A.1}$$

where R_1 is the tracer delivery ratio between the tissue of interest and the reference region. This ratio is defined as $R_1 = \frac{K_1}{K_1'} = \frac{k_2}{k_2'}$ where K_1 and k_2

(resp. K_1' and k_2') are the rate constants characterizing the exchange between the blood and the non-specific tissue of the target region (resp. the reference region). Moreover, in (A.1), the other model parameters are defined as

$$b_1 = \frac{(k_3 + k_4 - \alpha_1)(\alpha_1 - k_2/R_1)}{\sqrt{(k_2 + k_3 + k_4)^2 - 4k_2k_4}}, \tag{A.2}$$

$$b_2 = \frac{(\alpha_2 - k_3 - k_4)(\alpha_2 - k_2/R_1)}{\sqrt{(k_2 + k_3 + k_4)^2 - 4k_2k_4}}. \tag{A.3}$$

and

$$\alpha_1 = \frac{k_2 + k_3 + k_4 + \sqrt{(k_2 + k_3 + k_4)^2 - 4k_2k_4}}{2}, \tag{A.4}$$

$$\alpha_2 = \frac{k_2 + k_3 + k_4 - \sqrt{(k_2 + k_3 + k_4)^2 - 4k_2k_4}}{2}. \tag{A.5}$$

where k_3 and k_4 are rate constants associated with the kinetics between the non-specific and specific tissues of the target region. In particular, the binding potential is defined as $BP = \frac{k_3}{k_4}$. Gunn et al. (2001) further developed the binding potential relationship as

$$\mathrm{BP_{ND}} = \frac{K_1}{k_2}\left(1 + \frac{k_3}{k_4}\right)\left(\frac{K_1'}{k_2'}\right)^{-1} - 1, \tag{A.6}$$

where ND is the nondisplaceable radioligand in tissue. This expression can be rewritten as

$$\mathrm{BP_{ND}} = R_1\left(1 + \frac{b_1}{\alpha_1} + \frac{b_2}{\alpha_2}\right) - 1, \tag{A.7}$$

which is the formulation adopted in (7).

It is worth noting that choosing a reference region with no SB is of prime importance to successfully apply this model. Moreover, the distribution volume in the tissue of interest has to equal that in the reference tissue, i.e., $\frac{K_1}{k_2} = \frac{k_1'}{k_2'}$. In the experiments described in Section 4, this model has been leveraged on to simulate realistic SB variations. Conversely the nSB TACs are extracted from a real PET scan and, therefore, are not simulated with this model. Therefore only the parameters k_j $(j = 1, \cdots, 4)$ related to SB are used.

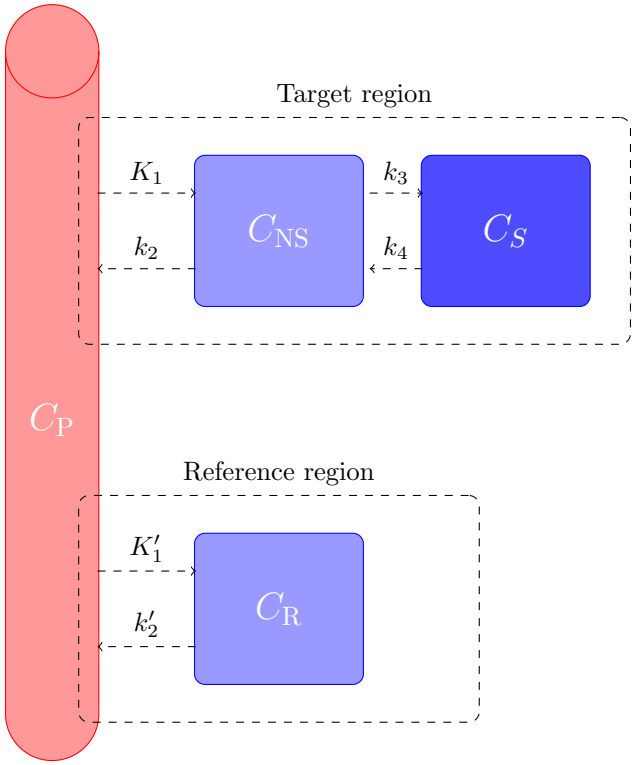

Figure A.12: Configuration of the conventional full reference tissue compartment model (see Häggström et al. (2016))

Appendix B. Algo. 1 – Optimization w.r.t. M

For $k = (1, \cdots, K-1)$, the required gradient is written

$$\begin{aligned}\nabla_{m_k}\mathcal{J}(\mathbf{m}_k, \mathbf{A}_k, \mathbf{W}_k, \mathbf{E}_k) = &-(\tilde{\mathbf{Y}} - \mathbf{m}_k\mathbf{A}_k)\mathbf{A}_k^T \\ &-\sum_{i=0}^{V}\mathbf{E}_{ki}^T\tilde{\mathbf{Y}}\mathbf{W}_{k,i}^T + \sum_{i=0}^{V}(\mathbf{E}_{ki} + \mathbf{E}_{ki}^T)\mathbf{m}_k\mathbf{W}_{k,i}\mathbf{A}_k^T \\ &+\frac{1}{2}\sum_{i=0}^{V}\sum_{j=0}^{V}(\mathbf{E}_{ki}^T\mathbf{E}_{kj} + (\mathbf{E}_{ki}^T\mathbf{E}_{kj})^T)(\mathbf{m}_k\mathbf{W}_{k,j}\mathbf{W}_{k,i}^T) \\ &+\beta(\tilde{\mathbf{M}} - \tilde{\mathbf{M}}^0)\end{aligned} \tag{B.1}$$

with $\tilde{\mathbf{Y}} = \mathbf{Y} - \sum_{j\neq k}\left(\mathbf{m}_j\mathbf{A}_j - \sum_{i=0}^{V}\mathbf{E}_{ji}\mathbf{m}_j\mathbf{W}_{ji}\right)$ and $\mathbf{W}_i = (\tilde{\mathbf{A}} \circ \mathbf{B}_i)$.
The Lipschitz constant is defined as

$$\begin{aligned}L_{m_k} = &\|\mathbf{A}_k\mathbf{A}_k^T\| + \sum_{i=0}^{V}\|\mathbf{E}_{ki} + \mathbf{E}_{ki}^T\|\|\mathbf{W}_{k,i}\mathbf{A}_k^T\| \\ &+\sum_{i=0}^{V}\sum_{j=0}^{V}\|\mathbf{E}_{ki}^T\mathbf{E}_{kj}\|\|\mathbf{W}_{k,j}\mathbf{W}_{k,i}^T\| + \beta\end{aligned} \tag{B.2}$$

where the spectral norm $\|\mathbf{X}\| = \sigma_{\max}(\mathbf{X})$ is the largest singular value of $\mathbf{X}$ and $\|\mathbf{X}\|_\infty = \max_{1\leq i\leq m}\sum_{j=1}^{n}|x_{ij}|$ is the sum of the absolute values of the matrix row entries.

For $k = K$, the gradient writes

$$\nabla_{m_K}\mathcal{J}(\mathbf{m}_K, \mathbf{A}_K) = -(\tilde{\mathbf{Y}} - \mathbf{m}_K\mathbf{A}_K)\mathbf{A}_K^T + \beta(\mathbf{m}_K - \mathbf{m}_K^0)$$

with $\tilde{\mathbf{Y}} = \mathbf{Y} - \tilde{\mathbf{M}}\tilde{\mathbf{A}} - \sum_{i=0}^{V}\mathbf{Q}_i(\tilde{\mathbf{A}} \circ \mathbf{B}_i)$. The Lipschitz constant is

$$L_{m_K} = \|\mathbf{A}_K\mathbf{A}_K^T\| + \beta.$$

Appendix C. Algo. 1 – Optimization w.r.t. A

For $\tilde{\mathbf{A}}$, the gradient can be computed as

$$\begin{aligned}\nabla_{\tilde{A}}\mathcal{J}(\tilde{\mathbf{M}}, \tilde{\mathbf{A}}, \mathbf{Q}, \mathbf{B}) = &-\tilde{\mathbf{M}}^T\tilde{\mathbf{Y}} - \sum_{j=0}^{V}\left((\mathbf{Q}_j^T\tilde{\mathbf{Y}}) \circ \mathbf{B}_j\right) \\ &+\eta\tilde{\mathbf{A}}\mathbf{S}\mathbf{S}^T\end{aligned} \tag{C.1}$$

with $\tilde{\mathbf{Y}} = \mathbf{Y} - \mathbf{MA} - \sum_{i=0}^{V} \mathbf{Q}_i(\tilde{\mathbf{A}} \circ \mathbf{B}_i)$ and $\tilde{\mathbf{M}} = [\mathbf{m}_1, \cdots, \mathbf{m}_{K-1}]$.

The corresponding Lipschitz constant is defined as

$$L_{\tilde{A}} = \sum_{i=0}^{V} \left(2\|\tilde{\mathbf{M}}^T \mathbf{Q}_i\| \|\mathbf{B}_i\| + \|\mathbf{B}_j\| \sum_{j=0}^{V} \|\mathbf{Q}_j^T \mathbf{Q}_i\| \|\mathbf{B}_i\| \right) + \|\tilde{\mathbf{M}}^T \tilde{\mathbf{M}}\| + \eta \|\mathbf{S}\mathbf{S}^T\|. \tag{C.2}$$

For $\mathbf{A}_K$, the gradient writes

$$\nabla_{A_K} \mathcal{J}(\mathbf{m}_K, \mathbf{A}_K) = -\mathbf{m}_K^T \tilde{\mathbf{Y}} + \eta \mathbf{A}_K \mathbf{S}\mathbf{S}^T$$

with $\tilde{\mathbf{Y}} = \mathbf{Y} - \mathbf{MA} - \sum_{i=0}^{V} \mathbf{Q}_i(\tilde{\mathbf{A}} \circ \mathbf{B}_i)$. The Lipschitz constant is

$$L_{A_K} = \|\mathbf{m}_K^T \mathbf{m}_K\| + \eta \|\mathbf{S}\mathbf{S}^T\|.$$

The Lipschitz constant is given by

$$L_{B_i} = \|\mathbf{Q}_i^T \mathbf{Q}_i\| \|\tilde{\mathbf{A}}\|^2. \tag{C.3}$$

Appendix D. Algo. 1 – Optimization with respect to $\mathbf{B}_i$

The gradient writes

$$\nabla_{B_i} \mathcal{J}(\tilde{\mathbf{A}}, \mathbf{B}, \mathbf{Q}) = -\left((\mathbf{Q}_i^T (\tilde{\mathbf{Y}} - \mathbf{Q}_i(\tilde{\mathbf{A}} \circ \mathbf{B}_i))) \circ \tilde{\mathbf{A}} \right) \tag{D.1}$$

with $\tilde{\mathbf{Y}} = \mathbf{Y} - \mathbf{MA} - \sum_{j \neq i} \mathbf{Q}_j(\tilde{\mathbf{A}} \circ \mathbf{B}_j)$.

The Lipschitz constant is

$$L_{B_i} = \|\mathbf{Q}_i^T \mathbf{Q}_i\| \|\tilde{\mathbf{A}}\|^2. \tag{D.2}$$

Appendix E. Algo. 1 – Optimization with respect to α_{ki}

The gradient writes

$$\nabla_{\alpha_{ki}} \mathcal{J}(\alpha_{ki}) = \mathbf{W}_{k,i} (\tilde{\mathbf{Y}}^T (T_p(\mathbf{t}) \circ \mathbf{E}_{ki}) - \frac{1}{2} \mathbf{W}_{k,i}^T \mathbf{m}_k^T ((T_p(\mathbf{t}) \circ \mathbf{E}_{ki})^T \mathbf{E}_{ki} + \mathbf{E}_{ki}^T (T_p(\mathbf{t}) \circ \mathbf{E}_{ki}))) \mathbf{m}_k, \tag{E.1}$$

with $\tilde{\mathbf{Y}} = \mathbf{Y} - \mathbf{MA} - \sum_{j \neq i} \mathbf{Q}_j \mathbf{W}_j - \sum_{u \neq k} \mathbf{E}_{ui} \mathbf{m}_u \mathbf{w}_{ui}$.

The Lipschitz constant is

$$L_{\alpha_{ki}} = \|\mathbf{W}_{k,i}\| \left(\| -\tilde{\mathbf{Y}}^T + \frac{1}{2} \mathbf{W}_{k,i}^T \mathbf{m}_k^T \mathbf{E}_{ki}^T \| + \frac{3}{2} \|\mathbf{W}_{k,i}^T \mathbf{m}_k^T\| \|\mathbf{E}_{ki}\| \right) \|\mathbf{E}_{ki}\| \|T_p(\mathbf{t})\|^2 \|\mathbf{m}_k\|. \tag{E.2}$$

Table F.3: Parameter values used to generate the basis function for DEPICT for the real data.

0.206	0.406	0.606	0.805	1.005	1.205	1.405	1.605	1.804	2.004
2.204	2.404	2.604	2.803	3.003	3.203	3.403	3.603	3.802	4.002
4.202	4.402	4.601	4.801	5.001	5.201	5.401	5.600	5.800	6.000

Appendix F. Choice of basis functions for DEPICT for the real data

During the experiment on real data described in Section 5, the basis functions used by DEPICT has been chosen following the approach initially adopted by Gunn et al. (2002). In that paper, 31 basis functions were generated as logarithmically spaced from the decay constant value to 6 min^{-1}. Conversely, in the experiment conducted in Section 5, the image has been already corrected for decay. Thus, the decay constant has been removed, leading to a final set of 30 basis functions. The final values are reported in Table F.3.

References

Altmann, Y., Dobigeon, N., Tourneret, J.-Y., June 2011. Bilinear models for nonlinear unmixing of hyperspectral images. In: Proc. IEEE GRSS Workshop Hyperspectral Image SIgnal Process.: Evolution in Remote Sens. (WHISPERS). Lisbon, Portugal, pp. 1–4.

Barber, D. C., 1980. The use of principal components in the quantitative analysis of gamma camera dynamic studies. Physics Med. Biol. 25 (2), 283–292.

Berti, V., Polito, C., Ramat, S., Vanzi, E., De Cristofaro, M. T., Pellicanò, G., Mungai, F., Marini, P., Formiconi, A. R., Sorbi, S., Pupi, A., March 2010. Brain metabolic correlates of dopaminergic degeneration in de novo idiopathic Parkinson's disease. Eur. J. Nuclear Med. Molecular Imag. 37 (3), 537–544.

Bioucas-Dias, J. M., Figueiredo, M. A. T., 2010. Alternating direction algorithms for constrained sparse regression: Application to hyperspectral unmixing. In: Proc. IEEE GRSS Workshop Hyperspectral Image SIgnal Process.: Evolution in Remote Sens. (WHISPERS).

Bioucas-Dias, J. M., Plaza, A., Dobigeon, N., Parente, M., Du, Q., Gader, P., Chanussot, J., April 2012. Hyperspectral unmixing overview: Geometrical, statistical, and sparse regression-based approaches. IEEE J. Sel. Topics Appl. Earth Observations Remote Sens. 5 (2), 354–379.

Blomqvist, G., Pauli, S., Farde, S., Eriksson, L., Person, A., Halldin, C., 1989. Dynamic models for reversible ligand binding. In: Positron emission tomography in clinical research and clinical diagnosis: tracer modelling and radioreceptors. INIS, pp. 35–44.

Boellaard, R., Turkheimer, F. E., Hinz, R., Schuitemaker, A., Scheltens, P., van Berckel, B. N. M., Lammertsma, A. A., Oct. 2008. Performance of a modified supervised cluster algorithm for extracting reference region input functions from (r)-[11c]pk11195 brain pet studies. In: Proc. IEEE Nuclear Sci. Symp (NSS). pp. 5400–5402.

Bolte, J., Sabach, S., Teboulle, M., July 2013. Proximal alternating linearized minimization for nonconvex and nonsmooth problems. Math. Programming 146 (1-2), 459–494.

Buckley, D. L., 2002. Uncertainty in the analysis of tracer kinetics using dynamic contrast-enhanced T1-weighted MRI. Magn. Reson. Med. 47 (3), 601–606.

Buvat, I., 2007. Quantification in emission tomography: Challenges, solutions, and performance. Nuclear Instruments and Methods in Physics Research Section A: Accelerators, Spectrometers, Detectors and Associated Equipment 571 (1), 10 – 13.

Cavailloles, F., Bazin, J. P., Di Paola, R., 1984. Factor analysis in gated cardiac studies. J. Nuclear Med. 25, 10671079.

Cavalcanti, Y. C., Oberlin, T., Dobigeon, N., Févotte, C., Stute, S., Ribeiro, M., Tauber, C., Sept. 2019. Factor analysis of dynamic PET images: beyond Gaussian noise. IEEE Trans. Med. Imaging 38 (9), 2231–2241.

Cavalcanti, Y. C., Oberlin, T., Dobigeon, N., Stute, S., Ribeiro, M., Tauber, C., 2018. Unmixing dynamic PET images with variable specific binding kinetics. Med. Image Analysis 49, 117 – 127.

Chen, L., Choyke, P. L., Chan, T. H., Chi, C. Y., Wang, G., Wang, Y., Dec. 2011. Tissue-specific compartmental analysis for dynamic contrast-enhanced MR imaging of complex tumors. IEEE Trans. Med. Imag. 30 (12), 2044–2058.

Condat, L., Sept. 2015. Fast projection onto the simplex and the l_1-ball. Math. Programming 158 (1-2), 575–585.

Cunningham, V. J., Hume, S. P., Price, G. R., Ahier, R. G., Cremer, J. E., Jones, A. K., 1991. Compartmental analysis of diprenorphine binding to opiate receptors in the rat in vivo and its comparison with equilibrium data in vitro. J. Cereb. Bl. Flow Metab. 11 (1), 1–9.

DeLorenzo, C., Kumar, J. D., Zanderigo, F., Mann, J. J., Parsey, R. V., 2009. Modeling considerations for in vivo quantification of the dopamine transporter using [11c] PE2I and positron emission tomography. J. Cereb. Bl. Flow Metab. 29 (7), 1332–1345.

Dobigeon, N., Moussaoui, S., Coulon, M., Tourneret, J.-Y., Hero, A., Nov. 2009. Joint Bayesian endmember extraction and linear unmixing for hyperspectral imagery. IEEE Trans. Signal Process. 57 (11), 4355–4368.

Dobigeon, N., Tits, L., Somers, B., Altmann, Y., Coppin, P., June 2014a. A comparison of nonlinear mixing models for vegetated areas using simulated and real hyperspectral data. IEEE J. Sel. Topics Appl. Earth Observations Remote Sens. 7 (6), 1869–1878.

Dobigeon, N., Tourneret, J.-Y., Richard, C., Bermudez, J. C. M., McLaughlin, S., Hero, A. O., 2014b. Nonlinear unmixing of hyperspectral images: Models and algorithms. IEEE Signal Process. Mag. 31 (1), 82–94.

Eches, O., Guillaume, M., April 2014. A bilinear-bilinear nonnegative matrix factorization method for hyperspectral unmixing. IEEE Geosci. Remote Sens. Lett. 11 (4), 778–782.

El Fakhri, G., Kardan, A., Sitek, A., Dorbala, S., Abi-Hatem, N., Lahoud, Y., Fischman, A., Coughlan, M., Yasuda, T., Di Carli, M. F., 2009. Reproducibility and accuracy of quantitative myocardial blood flow assessment with 82rb pet: Comparison with 13n-ammonia pet. J. Nuclear Med. 50 (7), 1062–1071.

El Fakhri, G., Sitek, A., Gurin, B., Kijewski, M. F., Di Carli, M. F., Moore, S. C., Aug. 2005. Quantitative dynamic cardiac $82^r b$ PET using generalized factor and compartment analyses. J. Nuclear Med. 46 (8), 1264–1271.

Emond, P., Guilloteau, D., Chalon, S., 2008. PE2I: A radiopharmaceutical for in vivo exploration of the dopamine transporter. CNS Neuroscience & Therapeutics 14 (1), 47–64.
URL https://onlinelibrary.wiley.com/doi/abs/10.1111/j.1527-3458.2007.00033.x

Erlandsson, K., Buvat, I., Pretorius, P. H., Thomas, B. A., Hutton, B. F., 2012. A review of partial volume correction techniques for emission tomography and their applications in neurology, cardiology and oncology. Physics in Medicine & Biology 57 (21), R119.

Fan, W., Hu, B., Miller, J., Li, M., 2009. Comparative study between a new nonlinear model and common linear model for analysing laboratory simulated-forest hyperspectral data. Int. J. Remote Sens. 30 (11), 2951–2962.

Ferraris, V., Dobigeon, N., Wei, Q., Chabert, M., April 2017. Robust fusion of multi-band images with different spatial and spectral resolutions for change detection. IEEE Trans. Comput. Imag. 3 (2), 175–186.

Gunn, R. N., Gunn, S. R., Cunningham, V. J., 2001. Positron emission

tomography compartmental models. J. Cereb. Bl. Flow Metab. 21 (6), 635–652.

Gunn, R. N., Gunn, S. R., Turkheimer, F. E., Aston, J. A. D., Cunningham, V. J., 2002. Positron emission tomography compartmental models: A basis pursuit strategy for kinetic modeling. J. Cereb. Bl. Flow Metab. 22 (12), 1425–1439.

Häggström, I., Beattie, B. J., Schmidtlein, C. R., 2016. Dynamic PET simulator via tomographic emission projection for kinetic modeling and parametric image studies. Med. Physics 43 (6), 3104–3116.

Heylen, R., Parente, M., Gader, P., 2014. A review of nonlinear hyperspectral unmixing methods. IEEE J. Sel. Topics Appl. Earth Observations Remote Sens. 7 (6), 1844–1868.

Huang, S. C., Phelps, M. E., Hoffman, E. J., Sideris, K., Selin, C. J., Kuhl, D. E., 1980. Noninvasive determination of local cerebral metabolic rate of glucose in man. Amer. J. Physiology-Endocrinology and Metabolism 238 (1), E69–E82.

Huang, S.-C., Zhou, Y., June 1998. Spatially-coordinated regression for image-wise model fitting to dynamic PET data for generating parametric images. IEEE Trans. Nuclear Sci. 45 (3), 1194–1199.

Innis, R. B., Cunningham, V. J., Delforge, J., Fujita, M., Gjedde, A., Gunn, R. N., Holden, J., Houle, S., Huang, S.-C., Ichise, M., et al., May 2007. Consensus nomenclature for in vivo imaging of reversibly binding radioligands. J. Cereb. Bl. Flow Metab. 27 (9), 1533–1539.

Kamasak, M. E., Bouman, C. A., Morris, E. D., Sauer, K., May 2005. Direct reconstruction of kinetic parameter images from dynamic PET data. IEEE Trans. Med. Imag. 24 (5), 636–650.

Klein, R., Beanlands, R. S., Wassenaar, R. W., Thorn, S. L., Lamoureux, M., DaSilva, J. N., Adler, A., deKemp, R. A., 2010. Kinetic model-based factor

analysis of dynamic sequences for 82-rubidium cardiac positron emission tomography. Med. Physics 37 (8), 3995–4010.

Lammertsma, A. A., Hume, S. P., 1996. Simplified reference tissue model for PET receptor studies. NeuroImage 4 (3), 153–158.

Lin, Y., Haldar, J. P., Li, Q., Conti, P. S., Leahy, R. M., Jan. 2014. Sparsity constrained mixture modeling for the estimation of kinetic parameters in dynamic PET. IEEE Trans. Med. Imag. 33 (1), 173–185.

Meganem, I., Dliot, P., Briottet, X., Deville, Y., Hosseini, S., Jan. 2014. Linear-quadratic mixing model for reflectances in urban environments. IEEE Trans. Geosci. Remote Sens. 52 (1), 544–558.

Nijran, K. S., Barber, D. C., 1985. Towards automatic analysis of dynamic radionuclide studies using principal-components factor analysis. Physics Med. Biol. 30 (12), 1315.

Padhani, A., 2003. MRI for assessing antivascular cancer treatments. The British Journal of Radiology 76 (suppl_1), S60–S80.

Padhani, A. R., Husband, J. E., 2001. Dynamic contrast-enhanced mri studies in oncology with an emphasis on quantification, validation and human studies. Clinical radiology 56 (8), 607–620.

Paola, R. D., Bazin, J. P., Aubry, F., Aurengo, A., Cavailloles, F., Herry, J. Y., Kahn, E., Aug. 1982. Handling of dynamic sequences in nuclear medicine. IEEE Trans. Nuclear Sci. 29 (4), 1310–1321.

Peng, J. Y., Aston, J. A. D., Gunn, R. N., Liou, C. Y., Ashburner, J., Sept. 2008. Dynamic positron emission tomography data-driven analysis using sparse Bayesian learning. IEEE Trans. Med. Imag. 27 (9), 1356–1369.

Polymeri, E., Sadik, M., Kaboteh, R., Borrelli, P., O, O. E., Uln, J., Ohlsson, M., Trgrdh, E., Poulsen, M., Simonsen, J., Hoilund-Carlsen, P. F., Johnsson, A., Edenbrandt, L., 2020. Deep learning-based quantification of pet/ct prostate

gland uptake: association with overall survival. Clin Physiol Funct Imaging 40 (), 103–113.

Sitek, A., Di Bella, E. V. R., Gullberg, G. T., 2000. Factor analysis with a priori knowledge – Application in dynamic cardiac SPECT. Physics Med. Biol. 45, 2619–2638.

Szabo, Z., Ravert, H. T., Gzkara, I., Geckle, W., Seki, C., Sostre, S., Peller, P., Monsein, L., Natarajan, T. K., Links, J. M., Wong, D. F., Dannals, R. F., Wagner, H. N., 1993. Noncompartmental and compartmental modeling of the kinetics of carbon-11 labeled pyrilamine in the human brain. Synapse 15 (4), 263–275.

Wang, B., Ruan, D., Liu, H., 2020. Noninvasive estimation of macro-parameters by deep learning. IEEE Transactions on Radiation and Plasma Medical Sciences 4 (6), 684–695.

Winter, M. E., 1999. N-FINDR: an algorithm for fast autonomous spectral end-member determination in hyperspectral data. In: Proc. SPIE Imaging Spectrometry V. Vol. 3753. pp. 266–275.

Yang, J., Huang, S., Mega, M., Lin, K., Toga, A., Small, G., Phelps, M., 1996. Investigation of partial volume correction methods for brain FDG PET studies. IEEE Trans. Nuclear Science 43 (6), 3322–3327.

Zubal, I. G., Harrell, C. R., Smith, E. O., Rattner, Z., Gindi, G., Hoffer, P. B., 1994. Computerized three-dimensional segmented human anatomy. Med. Physics 21 (2), 299–302.